

Buoyancy Considerations in a Fluidized Bed of Ground Particles

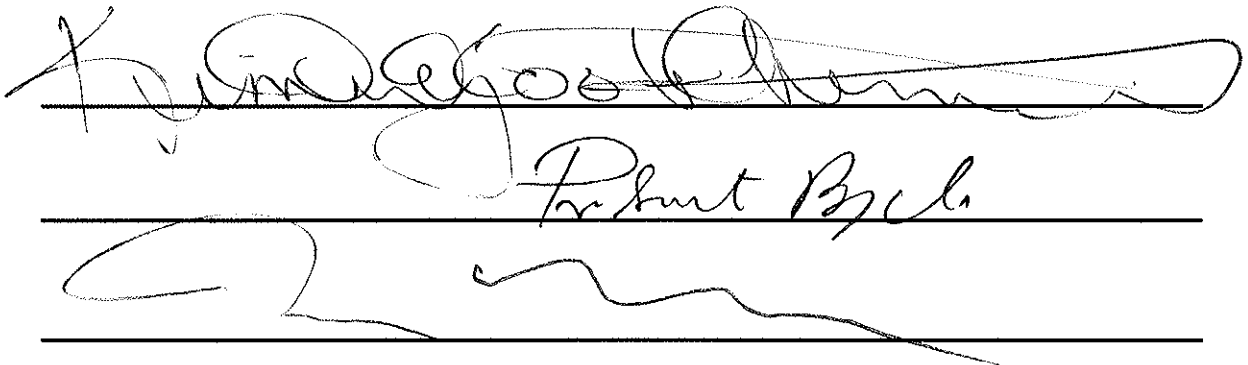
By Prakash R. Rao

A thesis submitted to the
Graduate School – New Brunswick
Rutgers, The State University of New Jersey
in partial fulfillment of the requirements
for the degree of
Master of Science

Graduate Program in Mechanical and Aerospace Engineering

Written under the direction of Professor Michael R. Muller

and approved by



The image shows three handwritten signatures on horizontal lines. The top signature is a long, flowing cursive script. The middle signature is written in a more stylized, blocky cursive and includes the name 'Prakash Rao'. The bottom signature is a shorter, more compact cursive script.

New Brunswick, New Jersey

October 2009

Buoyancy Considerations in a Fluidized Bed of Ground Particles

by
Prakash R. Rao

A thesis submitted to the
Graduate School – New Brunswick
Rutgers, The State University of New Jersey
in partial fulfillment of the requirements
for the degree of
Master of Science
Graduate Program in Mechanical and Aerospace Engineering

Written under the direction of
Professor Michael R. Muller

And approved by

New Brunswick, New Jersey

October 2009

Abstract of the Thesis

Buoyancy Considerations in a Fluidized Bed of Ground Particles

By Prakash R. Rao

Dissertation Director:

Dr. Michael R. Muller

The research conducted for this thesis determines and quantifies the forces acting on a large submerged object in a gas-solid fluidized bed of Geldart A ground particles at the onset of bubbling. In particular, the additional load from the previously reported de-fluidized region of particles found above submerged objects in fluidized beds is quantified. A force model was developed and comparisons between this and the experimental data yielded properties of the de-fluidized region, such as the shape and height of the hood, and the angle to which it rises. Drag is measured by comparing forces on objects of different geometries subject to the same conditions. Buoyancy was measured by summing the pressure force acting to push the submerged object out of the bed and the counteracting pressure force of the bed over the submerged object pushing it deeper into the bed. The de-fluidized region is found to have a significant impact on the buoyancy of the object by creating an additional weight force above the object thus increasing the pressure in this region. Explanations for the hood shape and size are made through phenomenological results obtained through visual observations. Particle transport through voidage collapses at the surface, i.e. “bubbling”, create a secondary particle circulation within the bed adding particles to the top of the hood. The size of the bubbles appears to determine the extent of the hood.

Acknowledgements

First and foremost, I would like to thank my adviser Dr. Michael R. Muller whose mentoring, efforts, dedication, guidance and patience led to the completion of this thesis.

I would also like to thank John Petrowski for all his help in building my several experimental set-ups.

I would like to thank the CAES graduate students, Sachin Nimbalkar, Malik Khan, Sara Salahi, Blake Boyer and Matt Schaefer as well as the CAES staff, Jill Mesonas, Josh Kace, Mike B. Muller, Don Kasten and Siddika Pasi and the several CAES undergraduates for all their support and good cheer.

Finally, I give grateful acknowledgment to my family – my lady and wife Simana Rao, whose support and patience saw me through this work and my parents, Raghavendra and Srivalli Rao and brother Prashant Rao whose guidance throughout led me here today.

Table of Contents

ABSTRACT OF THE THESIS.....	ii
ACKNOWLEDGEMENTS.....	iii
TABLE OF CONTENTS.....	iv
LIST OF FIGURES	v
CHAPTER 1 INTRODUCTION	1
1.1 DEFINITION OF TERMS	3
1.2 MOTIVATION FOR RESEARCH	6
1.3 LITERATURE REVIEW:	7
CHAPTER 2 EXPERIMENTAL SET-UP.....	21
2.1 GENERAL SET-UP	22
2.1.1 <i>Fluidized Bed</i>	22
2.1.2 <i>Ground Particles</i>	25
2.1.3 <i>Large Submerged Objects</i>	26
2.2 DETERMINATION OF THE PRESSURE DROP THROUGH THE BED	27
2.3 BED HEIGHT RISE ASSOCIATED WITH SUBMERSION OF SPHERE.....	28
2.4 FORCES ON SUBMERGED OBJECTS IN A FLUIDIZED BED	33
CHAPTER 3: RESULTS.....	38
3.1 DETERMINATION OF PRESSURE DROP THROUGH THE BED.....	38
3.3 FORCES ON AN OBJECT SUBMERGED IN A FLUIDIZED BED:	44
CHAPTER 4 THEORETICAL MODEL.....	48
4.1 DETERMINATION OF FORM DRAG.....	48
4.2 DETERMINATION OF BUOYANT FORCE	51
4.3 SKIN FRICTION DETERMINATION.....	54
4.4 DETERMINATION OF DE-FLUIDIZED HOOD WEIGHT AND SHAPE	60
4.5 SUMMATION OF MODEL FORCES	65
CHAPTER 5 CONCLUSIONS	66
5.1 COMPARISON TO PAST WORK	66
5.2 DISCUSSION ON HOOD SHAPE.....	70
NOMENCLATURE.....	76
REFERENCES.....	78

LIST OF FIGURES

FIGURE 1: COMPARISON OF STOKES DRAG ON A SPHERE TO EXPERIMENTAL RESULTS FOR DRAG ON A SPHERE IN A FLUIDIZED BED (JACKSON 2000)	8
FIGURE 2: DE-FLUIDIZED HOOD GROWTH WITH TIME (LEFT) AND PARTICLE MOVEMENT WITHIN (RIGHT). FROM HAGER AND SCHRAG (1975).....	17
FIGURE 3: SCHEMATIC OF BASIC FLUIDIZED BED SET-UP	23
FIGURE 4: PICTURE OF FLUIDIZED BED SET-UP.....	24
FIGURE 5: PACKING AND SETTLING OF ROUNDED SPHERES AND GROUND PARTICLES....	25
FIGURE 6: LARGE OBJECTS SUBMERGED IN BED. CYLINDER WITH ROUNDED END AND SPHERE	27
FIGURE 7: UNSLIDE ASSEMBLY	29
FIGURE 1: SCHEMATIC OF SET-UP FOR BED HEIGHT MEASUREMENT.....	30
FIGURE 2: PICTURE OF BED HEIGHT MEASUREMENT ASSEMBLY.....	31
FIGURE 10: TOP-DOWN VIEW OF BED HEIGHT MEASUREMENT ASSEMBLY.....	32
FIGURE 11: DATA FOR CALIBRATION OF PHOTODIODE	33
FIGURE 12: SET-UP FOR EXPERIMENTS MEASURING FORCES ON SUBMERGED OBJECTS	35
FIGURE 13: PICTURE OF ASSEMBLY FOR MEASURING FORCES ON SUBMERGED OBJECTS SHOWN OUTSIDE OF BED.....	36
FIGURE 14: PICTURE OF ASSEMBLY FOR MEASURING FORCES ON SUBMERGED OBJECTS SHOWN INSIDE BED.....	37
FIGURE 15: PRESSURE ACROSS BED VS. FLUIDIZED BED HEIGHT	38
FIGURE 16: BED HEIGHT RISE AS A SPHERE IS SUBMERGED INTO THE BED	40
FIGURE 17: BED HEIGHT CHANGE DURING FLUIDIZATION AND DE-FLUIDIZATION	42
FIGURE 19: FORCE ON SPHERE AND CYLINDER IN FLUIDIZED BED.....	45
FIGURE 20: FORM DRAG ON A SUBMERGED SPHERE.....	51
FIGURE 21: PRESSURE FORCE PUSHING SUBMERGED OBJECT UP AND OUT OF BED.....	54
FIGURE 22: SKIN FRICTION ON CYLINDER COMPARED TO THEORETICAL SKIN FRICTION..	57

FIGURE 23: PREDICTED FORCE ON CYLINDER COMPARED TO EXPERIMENTAL FORCE	58
FIGURE 24: PREDICTION OF SKIN FRICTION ON SPHERE AT 1.5UMF FLOW	59
FIGURE 25: 10TH DEGREE POLYNOMIAL TREND LINE FIT TO AVERAGE DATA FOR 1.5 UMF SPHERE	61
FIGURE 26: FORCE FROM ABOVE ON SPHERE	62
FIGURE 27: HOOD SHAPE EXTRACTED FROM HOOD WEIGHT DATA	64
FIGURE 28: COMPARISON OF MODEL TO DATA FOR 1.5 UMF FLOW SPHERE CASE	65
FIGURE 29: COMPARISON OF HOOD SHAPES	67
FIGURE 30: COMPARISON OF MODEL TO GRACE AND HOSNEY FOR 1.5 UMF CASE	70
FIGURE 31: HOOD AT 1R, 2R, 2.94R, 3.34R, 3.61R, 4.16R.....	72
FIGURE 32: DIAGRAM OF THE SECONDARY CIRCULATION LEADING THE DE-FLUIDIZED HOOD GROWTH.	74

Chapter 1 Introduction

A fluidized bed is a quasi-fluid made up of particles suspended by an upward flow of gas. Fluidization deviates from percolation in that that fluid flow is sufficient enough to match the particles terminal velocity, whereas in percolation the bed remains unmoved and the air flows through interstitial space. Fluidized beds are created using cylindrical chambers that hold a granular medium with an air flow passing through a perforated sheet and rising through the medium. If there is an obstruction to the gas flow within the bed, such as heat exchanger tubes or bubbles, then there is a tendency for a stagnant, dead region of particles to form above these obstructions. This region can have a significant impact on heat transfer coefficients (in the case of heat exchanger tubes), bubble rise time (in the case of bubbles) and in general the apparent buoyancy of submerged objects. The goals of the thesis are to experimentally determine the weight, size and shape of the stagnant region, henceforth referred to as the “de-fluidized hood”.

Fluidized beds are not a new technology but have been studied and used for coal combustion and particle drying since the 1940s. Fluidized beds represent a clean method of burning coal efficiently. The particles are small enough to be suspended, thus exposing more surface area than a lump of coal, but large enough such that they can be treated as a lumped mass. The particles effectively act as a thermal mass keeping the fluidized bed combustion chamber at a uniform temperature. This allows the operator to run the bed at lower temperatures than those seen in pulverized coal plants. Fluidized bed temperatures are on the order of 700°C - 800°C . This is below the temperature at which thermal NO_x forms. Additionally, limestone can easily be added to the fluidized coal particles to

remove SO_x gases from the exhaust. The result of combining the limestone with SO_x is gypsum, which is a profitable by-product.

Due to static electric forces within the bed, particles can be drawn together and form loose bonds [Mehrani 2004]. They can agglomerate thus reducing the particles capacity to act as a thermal mass, in addition to altering the conditions under which the bed will fluidize. The result is a fluidized bed operating under suboptimal conditions. A ‘mixer’ that could mechanically break up these agglomerations would reduce the negative effects of particle agglomeration.

The agglomeration of particles is one manner in which a fluidized bed differs from a fluid. However, in many other ways, the bed will behave like a fluid. For example, if the bed is stirred with a pole, the pole will meet negligible resistance, akin to the resistance felt when stirring a pot of water. Similarly, if the bed is tilted, the surface will remain parallel to the floor and even. Likewise, an object denser than the fluid should sink, while an object less dense should sit at the surface.

The last point, however, is a source of peculiarity. Some objects of a density slightly less than that of the bed, if placed at the bottom of the bed will remain at the bottom of the bed. If the same object is placed on the surface of the bed, it will stay at the surface.

In an attempt to create an object that could break up agglomerates in a fluidized bed, it was hypothesized that an object of a density equivalent to that of the bed could be moved

up and down within the bed by changing the flow rate of gas to the bed thus altering the buoyant force on the object. A decrease in flow rate would increase the density of the bed, thus pushing the object towards the surface. Increasing the flow rate would do the opposite and decrease the density of the bed, thus pushing the object to the bottom of the bed. However, the hypothesis failed as objects that should float based on this idea did not float but rather sank. Thus, buoyancy was not the only force acting on the object. Upon further investigation, the role of the de-fluidized hood of settled particles accumulating above the object was found to be significant. It was altering the effect of buoyancy on submerged objects in fluidized beds by adding an additional mass to the object, and by changing the density of the fluid above the object.

This thesis aims to identify the forces experienced by large objects within a fluidized bed of ground particles, with a particular focus on the de-fluidized hood. Not only will an understanding of these forces lead to the creation of a mixer that can break agglomerates within the bed, it can also be used to help understand the motion of bubbles in a fluidized bed and the decrease in heat transfer coefficients for regions above heat exchanger tubes within a fluidized bed.

1.1 Definition of Terms

This section will serve to provide a short understanding of the relevant basic terms used in this thesis when discussing fluidized beds.

Initially, the fluidized bed is filled with sand (in this case, alumina oxide) with the air supply to the bed turned off. The height to which the sand fills the bed is referred to as the ‘dead bed height’ – with the term dead bed used to refer to the fluidized bed with less flow than that required to fluidize the sand.

As air is introduced to the bed, the bed of sand will slowly rise. It will first rise relatively calmly and the surface will remain flat. In order for the bed to fluidize, the flow rate must be sufficient enough to provide a pressure drop adequate to support the weight of the bed. This pressure can be expressed as (Howard 1989):

$$\Delta p_b = \frac{M}{\rho_p A} (\rho_p - \rho_g) g$$

Equation 1

Where p_b is the pressure drop through the bed, M is the mass of the particles, ρ_p is the density of the particles, ρ_g is the density of the gas, and g is the acceleration due to gravity.

The velocity at which the pressure drop condition is met is known as the ‘minimum fluidization velocity’. At this point, the particles ‘interstitial distance’, or the distance between each particle, will be at its final value. The term voidage, designated by the symbol ε , is used to describe the amount of gas within the total volume of the fluidized bed. The height to which the bed rises is referred to as the bed height. Any additionally flow will not increase the voidage or the bed height. Rather, increasing the flow beyond the minimum fluidization velocity will cause ‘bubbling’, or the escape of excess gas from

the bed through voids. At this point the bed surface will no longer behave calmly, but will resemble a pot of boiling water. If the flow rate is increased past that required for bubbling, the phenomenon of 'slugging' will occur, which is essentially large scale bubbling where the bubbles grow to have the same diameter as the bed.

Increasing the flow rate further will spew sand particles out of the bed. Operating the bed under conditions beyond gentle bubbling is of no value in the present work as the bed is far too unsteady for any valuable measurements to be made.

Upon collapsing at the surface, the bubbles release particles entrained in its wake. These particles are released towards the walls of the bed chamber. At the chamber walls, the gas velocity is zero due to the no-slip boundary condition at the wall. Therefore, particles at the wall, having no supporting force from the air, down-well to the bottom of the bed. At the bottom, they are re-entrained in the bubble path and travel back to the bed surface only to repeat their journey. This leads to a circulation of particles within a fluidized bed that is a key mechanism of particle mixing within a bed.

As is evident, in order for fluidization to exist, the flow must be allowed to pass through the sand. Any obstruction to the flow that would bring the flow locally to a value less than the minimum fluidization velocity would create a region of de-fluidization. This de-fluidized region will act as a packed bed, or dead bed.

Buoyancy, as it relates to an object in a static fluid, is calculated by integrating the pressure drop across the surface of the object. In a fluidized bed, the fluid is not static. There is still a pressure drop around a submerged object or particle. However, when the effect of the de-fluidized hood is included, the pressure drop around the object is no longer uniform. This must be taken into account when calculating the buoyancy of an object in a fluidized bed.

There is a force which is essentially the drag on the submerged object or particle within the fluidized bed. This drag force will act in exactly the same manner as traditional drag and will be subdivided into two categories: form drag and skin drag. Form drag is associated with the flow hitting the submerged object and changing direction due to the geometric obstruction that the object presents. Skin drag will be the resistance to motion due to friction. Thus, the bed will have an apparent viscosity, which will predominantly be due to the collision of sand particles against the object and the flow of air around it (Davidson 1977).

1.2 Motivation for Research

The research conducted for this thesis aims to determine and quantify the forces acting on a large submerged object in a gas-solid fluidized bed of ground particles. The larger goal is to create a geometry that can move up and down in a fluidized bed by adjusting the flow rate and break up any agglomerations while also mixing the particles within the bed.

Many studies have been conducted concerning forces on objects within a fluidized bed. However, these works differ from the current work because they used perfectly spherical particles, they did not take into account the de-fluidized hood, they used a rectangular two dimensional bed, they operated the bed at higher flow rates, or they studied forces on particles of equal size as the fluidizing medium.

Unlike in past works, experimental results will directly be used to calculate aspects of the hood. These properties include the approximate position along the submerged object at which the hood begins, the weight of the hood, the shape and height of the hood, and the angle to which it rises.

The present work will hopefully shed more light on the nature of the de-fluidized hood as there is limited available work on this topic. The current work hopes to enable future researchers to better grasp the interactions between the fluidized medium and large objects within the beds.

1.3 Literature Review:

Drag on particles in a fluidized bed has been well discussed in the literature. The most common treatment for beds under low Reynolds number flows has been to look at the well documented Stokes Drag on a sphere, where, for $Re < 1$, the drag coefficient, C_D , can be estimated as:

$$C_D = \frac{24}{Re}$$

Equation 2

However, experimental data from studies on drag coefficients shows that the above does not match well. In Crowe et al (1998) the data is summarized and compared to the standard drag curve. This has been reprinted in Figure 3. The lines resembling scratches are data points from previous researchers' work.

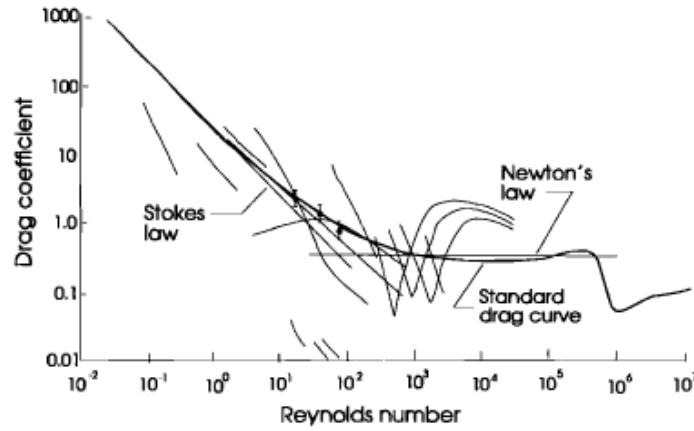


Figure 3: Comparison of Stokes Drag on a sphere to experimental results for drag on a sphere in a fluidized bed (Jackson 2000)

A correction for drag coefficient, f , for a particle under steady state has been given:

$$f = \frac{C_D Re_r}{24}$$

Equation 3

where Re_r is the Reynolds number based on the relative velocity of the gas to the particles.

Clift and Gauvin (1970) give the following relation for f over the entire subcritical Re range:

$$f = 1 + 0.15 Re_r^{0.687} + 0.0175 Re_r (1 + 4.25 \times 10^4 Re_r^{-1.16})^{-1}$$

Equation 4

Other expressions for f have been made by other researchers. For example, Mostoufi and Chaouki (1999) studied a liquid solid fluidized bed and assumed the following for f :

$$f = \varepsilon^{-m}$$

Equation 5

The assumption here, which has been validated by others as will be described below, is that the drag will be heavily dependent on the bed voidage, where ε is the bed voidage. Through experimentation, an expression for the variable m was given:

$$m = 3.02 Ar^{0.22} Re^{-0.33} \left(\frac{d_m}{d_s} \right)^{0.40}$$

Equation 6

Where d_m is the particle diameter and d_s is the diameter of a particle with the same surface area as the actual particle. Here, they have expressed the drag coefficient as a function of both the particle Archimedes number and Reynolds number.

When discussing drag in a fluidized bed, an understanding of viscosity within a fluidized bed is necessary. Liu et al (1960) stirred a paddle in a fluidized bed of glass beads in an

attempt to measure the apparent viscosity of a gas-solid fluidized system. His results showed that viscosity would decrease as the gas flow rate was increased. He attributes this to particle number density. With low flow rates, the paddle would have to stir through more particles than it would at higher flow rates since the bed is less fluidized. This result is intuitive; a dense fluid is harder to stir through compared to a less dense fluid. Batchelor (1988) states the same conclusion; that the apparent viscosity will change with flow rate.

Davidson et al (1977) studied bubble rise in fluidized beds. The scenario is similar to the current study in that there is a large object – in the case of Davidson a void of air and in the present case a submerged sphere – experiencing forces from a fluidized bed. The chief difference is of course that the bubbles are in motion whereas the sphere is fixed. Davidson et al argued that traditional viscosity does not affect bubble rise in fluidized beds. However, he continues, data demonstrates the obvious existence of an apparent viscosity of a fluidized bed caused by particle collision from the dense phase on to other objects. He proposed that an average viscosity over all types of fluidizing mediums could be taken as being 1 kg/m-sec.

Buoyancy within a fluidized bed has been discussed at length in the literature as well but with ambiguity, as discussed by Jackson in 2000. He defines a force \mathbf{f} , which is the average value of the force on a fluid by a particle in the fluid. For a fluid at rest, this force is:

$$\mathbf{f} = V\nabla p = \rho_f V\mathbf{g}$$

Equation 7

Where V is the volume of the object immersed in the fluid, ∇p is the pressure gradient, ρ_f is the density of the fluidized bed and g is the acceleration due to gravity. The right hand side of the above equation is a statement of Archimedes principle, where the buoyant force is equivalent to the weight of the displaced fluid. The right hand side is also equal to the integral of the pressure over the surface of an object submerged in a liquid.

Jackson continues modifying the conditions of the above equation and ultimately describes the situation found in a fluidized bed where there is a flow through a uniform bed of particles with voidage ϵ . The fluid is subject to an acceleration a , which is defined as du/dt where u is the fluid velocity. The accelerating fluid exerts a force on the immersed object. As Jackson explains, the ambiguity in defining buoyancy arises in the treatment of the force contribution by the accelerating fluid; it can either be lumped together with the buoyant force or it can be treated as a separate force onto itself.

Furthermore, greater debate in the calculation of buoyancy arises concerning the density to be used in calculations. As Jackson explains, the bulk density, denoted here as the density of the fluidized bed, should be used rather than the fluid density if: 1) the weight of the particles is fully supported by the fluid flow and 2) the fluid is at rest or in uniform motion. The usage of the bulk density is not valid if either condition is not met. Mostoufi and Chaouki (1999) also summarize these arguments and state that one side believes the

bulk density should be used for all cases while the other side believes that bulk density should only be used when the particles are much smaller than the submerged object.

Batchelor (1988) clarifies the above. In developing the force balance for particles in a fluidized bed, he states that buoyancy is strictly the mean force exerted by particles on the fluid. However, for the sake of simplicity, he includes it in a term meant to represent the mean force on particles by gravity. Thus, he states the gravity force as:

$$g = AM\tilde{g} \int_{x_1}^{x_2} n dx$$

Equation 8

Where A is the cross sectional area of the bed, M is the mass of the particles, n is the particle number density and the limits of integration represent the positions of the upper and lower surfaces of the fluidized bed cylinder. The gravitational acceleration, \tilde{g} , is:

$$\tilde{g} = g \frac{\rho_p - \rho_g}{\rho_p}$$

Equation 9

Where ρ_p is the density of the particles, ρ_g is the density of the gas and g is the standard gravitational acceleration. The correction to the acceleration is used to account for the buoyant force.

Howard (1989) shows that the velocity at which particles will fluidize is based on the buoyant force. He rewrites the commonly used Ergun Equation, which provides a relation

for the pressure drop through a fluidized bed, in non-dimensional terms and solves for the Archimedes number, a non dimensional number that is essentially a balance between the buoyant forces to the viscous forces. The Ergun Equation is as follows:

$$\frac{\Delta p_b}{L} = 150 \frac{(1-\varepsilon)^2}{\varepsilon^2} \frac{\mu_f U}{(\phi d_m)^2} + 1.75 \frac{(1-\varepsilon)}{\varepsilon^2} \frac{\rho_f U^2}{\phi d_m}$$

Equation 10

Where Δp_b is the pressure drop through the bed, L is the bed height, ε is the bed voidage, μ_f is the fluid viscosity, U is the fluidization velocity, ϕ is the sphericity which is the ratio of the surface area of a sphere of the same volume as the particle to the surface area of the particle, ρ_f is the density of the fluidized bed and d_m is the mean particle diameter.

Howard non-dimensionalizes Equation 10 and rewrites it at the minimum fluidization velocity as

$$Ar = 150 \frac{(1-\varepsilon_{mf})}{\phi^2 \varepsilon_{mf}^3} Re_{mf} + \frac{1.75}{\phi \varepsilon_{mf}^3} Re_{mf}^2$$

Equation 11

Where Ar is the Archimedes number:

$$Ar = \frac{\rho_f (\rho_p - \rho_f) g d_m^3}{\mu_f^2}$$

Equation 12

And Re_{mf} is the Reynolds number at the minimum fluidization velocity:

$$\text{Re}_{mf} = \frac{\rho_f U_{mf} d_m}{\mu_f}$$

Equation 13

With this, the Archimedes number, which is a measure of magnitude of the buoyant forces, is expressed in terms of the Re_{mf} . The velocity at which Equation 11 is met will fluidize the bed. Therefore, the minimum fluidization velocity is dependent on the buoyant force on the particles.

The previous discussions on buoyancy dealt with it on theoretical terms. Many researchers have tried to experimentally measure the buoyant forces in a fluidized bed. Grace and Hosney in 1985 investigated the forces on horizontal tubes in a fluidized bed of spherical and non-spherical objects as bubbles passed by the tubes. The tubes were attached to the bed by two strain gauges at either end. The researchers were interested in discerning the effects of superficial gas velocity, static bed height, particle diameter, particle density, tube diameter and tube shape on the vertical forces on tubes. The conclusions reached are that the buoyant force at times when bubbles are not present is very nearly approximated by Archimedes Principle, but corrected by:

$$F_B = 0.7 \rho_s (1 - \varepsilon_{mf}) g V$$

Equation 14

Where F_B is the buoyant force, ρ_s is the density of the dead bed, ε_{mf} is the voidage at the minimum fluidization velocity and V is the displaced volume. Grace and Hosney attribute the factor of 0.7 “to the tendency for a ‘stagnant cap’ of particles to form on top of an immersed tube”. The coefficient of 0.7 was developed experimentally.

Additional studies on the apparent buoyancy of large spheres at several locations in fluidized beds were carried out by Oshitani et al (2000). The fluidizing medium was spherical glass beads. Their goal was to measure local particle flow velocities by measuring the buoyancy of a submerged object at different locations. Their experimental set-up was very similar to that of the present work, as will be explained later. However, they did not consider the effect of the de-fluidized region above the sphere, as mentioned by Grace and Hosney, and others (to be described forthcoming). Oshitani et al used the following relation to determine the buoyancy:

$$\text{Apparent Buoyant Force} = \frac{|\text{weight of sphere in atmosphere} - \text{weight of sphere in bed}|}{\text{weight of sphere in atmosphere}}$$

Equation 15

Their results showed marked variation in apparent buoyancy and thus flow velocity as particle size, superficial gas velocity and bed height are increased. Therefore, it can be assumed that the apparent buoyancy is a function of the studied parameters.

In relating buoyant forces to gas velocity, as Oshitani does, it may be pertinent to review the work of Tee et al (2007). Here, it has been shown that velocity fluctuations can be observed throughout a fluidized bed and can be attributed to density differences within a bed. Tee et al hypothesize that this is due to polydispersity of the particles. As studied by many researchers (Qiaoqun et al (2004), Marzochella et al (2000), Huilin et al (2003), Gilbertson et al (2001), Asif (1997)), particles in a fluidized bed will segregate based on their density differences with the denser particles settling to the bottom and less dense

particles rising to the top. If the particles are all of the same density but of different sizes, then, based on the mass of the particles, the smaller particles will be located at the top of the bed and the larger ones at the bottom of the bed. In the work of Tee et al, the velocities of the interstitial flow vary because fluidization velocities will be dependent on the density of the particles. He argued that the velocity fluctuations arise due to the particles trying to regain the balance between buoyancy (which is density dependent) and drag (which is velocity dependent). Implicit in this argument is the idea that the only two forces acting on a particle are buoyancy and drag.

The final force exerted on a submerged object by the fluidized bed will be that of the de-fluidized region. As stated by Grace and Hosney, a “stagnant cap” of particles sat on top of their tubes within the fluidized bed. Many researchers had previously studied the flow patterns and forces on objects immersed in a gas-solid fluidized bed.

Glass and Harrison (1964) studied the flow around solid obstacles in a fluidized bed. The fluidized bed was comprised of sand and the gas velocity was held to 2-3 times that of minimum fluidization. Their findings showed three regions of flow around the object: 1) an area of air immediately below the object 2) a seemingly de-fluidized region above the sphere and 3) chains of bubbles at the sides of the obstacle. They state that the de-fluidized region would most likely disappear at high gas flow rates.

Hager and Schrag (1975) studied the de-fluidized hood on fixed cylinders in a rectangular fluidized bed of uniform glass beads. The goal was to take photographs of the hood and

determine the particle motion within the hood. This was done by using tinted beads to initially form the cap and then tracking the tinted beads over time. The bed was fluidized under bubbling conditions. The resulting hood shape and growth with time is shown in Figure 4.

As one can see, the work of Hager and Schrag indicates that the hood is similar in size to a cone with a wide and rounded top (image on left of Figure 4). Also visible is the motion of the top layer of the hood. Over time it erodes until it is all but gone. However, as is evident from the image on right of Figure 4, the initial cap is replaced and “overturns”, meaning that new particles replace the previous particles. This leads to a constant hood shape. Thus, they report a secondary flow pattern within the bed causing particles to move inward toward the center of the bed. This would appear to be the mechanism by which the hood is sustained.

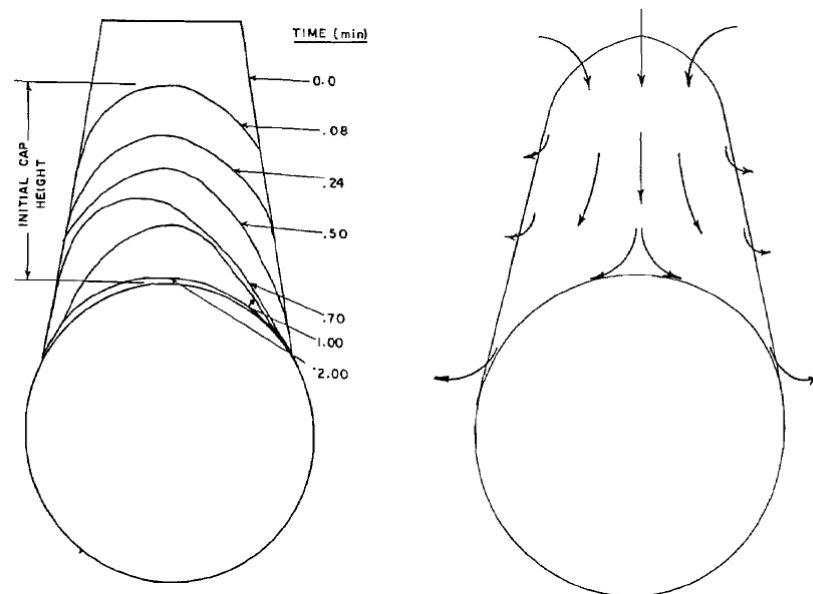


Figure 4: De-fluidized hood growth with time (left) and particle movement within (right). From Hager and Schrag (1975)

Hager and Schrag, based on their visual, found the ratio of the hood height to the object diameter to be 0.80. Other researchers reported values of 1 to 4, but these works did not have the benefit of tracking the hood.

Kulkarni (1986) also reported the same de-fluidized region. He looked at tubes immersed in a rectangular fluidized bed of spherical glass beads with air as the fluidizing gas. His objective was to study time averaged characteristics of properties of the hood such as height and its relation to fluidizing gas velocities and particle size using long exposure still photography. His photographs confirmed the existence of the de-fluidized hood. He also confirms the gap of air, as reported by Glass and Harrison, below the object. From his estimations of the hood height, Kulkarni proposes that the height of the hood is related to the fluidizing velocity by:

$$\frac{H_{hood}}{d} = 0.489 \left(\frac{U}{U_{mf}} \right)^{1.035}$$

Equation 16

With H_{hood} being the hood height, d being the diameter of the immersed object, U being the gas velocity and U_{mf} being the minimum fluidization velocity. The height of the hood decreases with increasing minimum fluidization velocity.

Additionally, A.C. Rees et al (2004) studied the rise of spheres in fluidized beds with air as the fluidizing medium. The bed was fluidized such that it was bubbling or slugging. Rees et al found that the spheres rose faster when subjected to higher gas velocities. Peculiarities were observed in that objects that were expected to rise based upon the

predicted density difference between the object and the fluidizing medium would sink. Furthermore, rise velocities were lower than the predicted rise velocities. These phenomena were attributed to the presence of the de-fluidized region above the spheres. Shapes and relations for the dimensions of the hood were derived assuming Stokes' flow. Rees et al concludes that the rise of buoyant objects in a fluidized bed can be predicted using Stokes's Law for a sphere moving in a viscous liquid.

Rees et al assumed the shape of the de-fluidized hood was that of a cylinder with a rounded end. The height of the hood was correlated to be:

$$H_{hood} = \frac{4 V_{HOOD}}{\pi d_{SPHERE}^2} + \frac{d}{2}$$

Equation 17

where V_{HOOD} is the volume of the hood and d is the diameter of the sphere. The volume of the hood was not directly calculated by Rees, but rather it was inferred from other calculations, such as relations he has given for the minimum fluidization velocity, total volume of the particle, shape factors proposed by Bowen and Masliyah (1973), and wall correction factors proposed by Perry and Green (1998). His relation for the minimum fluidization velocity is:

$$U_{mf} = \frac{g Vol_t (\rho_{g(mf)} - \rho_p) k_w}{3 \Delta \pi \mu_{f(mf)} d}$$

Equation 18

Where Vol_t is the total volume of the particle and hood, k_w is the wall correction factor, and Δ is a shape correction factor for the total particle. Rees et al provide relations for all of the unknowns in Equation 18 except $\mu_{f(mf)}$, the viscosity at minimum fluidization, and the volume of the hood, which, along with the volume of the submerged object, make up Vol_t . By taking two sets of data points, Rees et al can solve for these two unknowns. He finds the viscosity to be 0.66 Pa-s, which is in good agreement with the value proposed by Davidson (1977) and he finds that the hood height can be scaled with the diameter of the immersed object, as proposed by Hager and Schrag.

Rees, et al (2007) also took previous data from Daniels 1959 of falling spheres in a fluidized bed, introduced the concept of the de-fluidized hood and found good agreement between experimental data and theory for calculating apparent viscosities of a fluidized bed.

Chapter 2 Experimental Set-Up

Experiments were run to determine the pressure drop across the fluidized bed, the bed height increase due to the submersion of the sphere into the bath, the forces exerted on the sphere by the fluidized medium at different vertical positions within the bed, and the forces exerted on a cylinder with a rounded end at different vertical positions within the bed.

The basic experimental set-up consisted of a fluidized bed provided by the Techne Corporation. Air was fed using compressed air provided by Rutgers University. The volume flow rate of air and pressure were regulated through use of a rotameter and a pressure regulator respectively. Ground alumina oxide particles of Geldart A size were used as the fluidizing medium. Fluidization was maintained above the minimum fluidization velocity and at the onset of bubbling. This level was visually determined.

The pressure drop across the bed was calculated by measuring the increase in pressure as more alumina oxide was added to the bed. The increase in bed height due to the submersion of the sphere in the fluidized bath was measured using a photodiode with a strong light source and outputted to Labview software. The forces exerted by the fluidized bath on the sphere were determined by weighing the sphere as it was slowly submerged into the bed using a measuring system constructed out of two scales and a support beam. The forces exerted by the fluidized bath on a cylinder with a rounded end

were measured using the same scale apparatus used for measuring the forces on the sphere. A detailed explanation of all the components of the experiments follows.

2.1 General Set-up

2.1.1 Fluidized Bed

The fluidized bed, an FB-08 Fluidized Calibration Bath provided by the Techne Corporation, is made of stainless steel and has an inside diameter of 23 cm and height of 43.2 cm. The bed was oriented vertically and open to the atmosphere at the top. Air was fed into a plenum chamber through a 1/8" inlet. The inlet was located at the wall and air was injected into the plenum in the radial direction. The plenum was approximately 3.5 cm high. The plenum chamber buffered the air flow and dispersed it evenly through a perforated plate with holes less than 45 microns. Above the perforated plate was the fluidized medium.

The compressed air was provided by Rutgers University and was set at 85 psi. A valve first dropped the pressure to around 1 psi. The compressed air was then further regulated by a rotameter. The rotameter is essentially a valve with a maximum volume flow rate of 40 scfh. It could be set through the use of a dial that would open or close the valve. The instrument read out in percents of 40 scfh. A pressure gauge was located after the rotameter and before the air inlet to the fluidized bed. For the present experiments, the valve was opened one turn and air was turned on such that the rotameter read 100%. This

corresponded to a pressure of 0.79 psig and a flow rate of 40 scfh. Now the valve would be reduced to the desired flow rate. Setting the flow rate in this manner guaranteed that the pressure of the inlet air flow was kept constant from experiment to experiment. A schematic of the set-up can be seen in Figure 5.

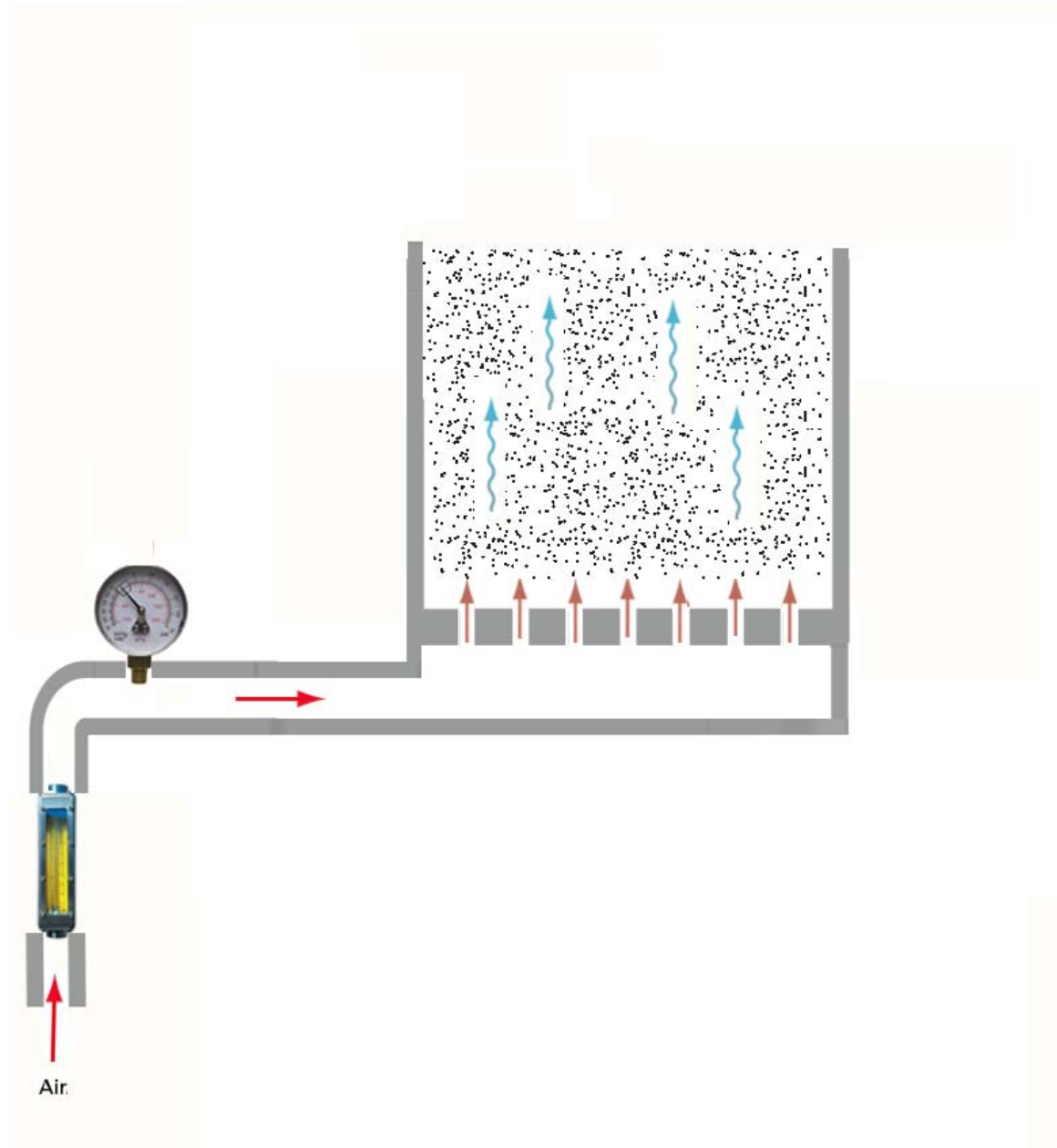


Figure 5: Schematic of basic fluidized bed set-up

A picture of the basic set-up can be seen in **Error! Reference source not found.** Figure 4.



Figure 6: Picture of fluidized bed set-up

2.1.2 Ground Particles

Ground alumina oxide (ranging in diameters from 45 to 125 microns) with a density of 963.1 kg/m^3 was used as the fluidizing medium. The particles were thus of Geldart size A. The bed was filled with enough alumina oxide such that the aspect ratio (ratio of height of the fluidized bed at incipient fluidization to the diameter of the bed) was kept at 1. This corresponded to 7.98 kg of sand. Ground particles rather than perfectly round ones were used in order to simulate the shape of particles commonly used in fluidized beds in industry. One difference between ground and round particles is the manner in which they settle or pack. Round particles will eventually settle in a uniform fashion with each particle touching four other particles at one contact point per adjacent particle. Ground particles will settle in an unpredictable fashion. This will make the interstitial distances between particles different locally, whereas the distance between adjacent spherical particles will be the same for all particles. Figure 5 has been provided to clarify this point:

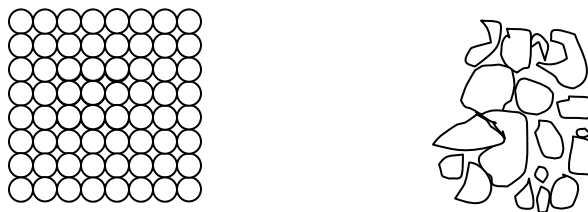


Figure 7: Packing and settling of rounded spheres (left) and ground particles (right)

Another difference between ground and round particles is the manner in which the flow moves around the particles. Ideally, the flow around each round particle should be the same whereas with ground particles, since no two particles are alike, the flow around each will be different.

Additionally, particles of different sizes were used. This allows for stratification of particles, as is commonly seen in industrial applications. Big particles will reside at the bottom of the bed while small particles will reside at the top. Although not studied in the present work and as previously stated, it has been hypothesized that stratification leads to variations in flow rate along the vertical axis of the bed and thus variations in bed density (Tee et al 2007). Density has a large roll in the forces exerted on submerged objects in fluidized beds. Using particles of varying sizes and shapes will better mimic real fluidized bed operating conditions.

2.1.3 Large Submerged Objects

A hard, hollow plastic sphere of radius $R_{\text{SPHERE}} = 4.775$ cm with negligible wall thickness was used as the large object submerged in the bed. The sphere had an approximately 1/16" hole made during its manufacturing. The hole was used to stake the sphere and attach it to various instruments that would move the sphere a measurable distance vertically. The sphere weighed 36 grams.

For experiments that were intended to eliminate the de-fluidized hood, the same sphere was used however a hollow cylinder made out of aluminum flashing was attached to the sphere. This is the “cylinder with rounded end” referred to in this thesis. The tube attached at the hemisphere, $R = R_{\text{SPHERE}}$, and the length was designed such that the whole apparatus would never be completely submerged. The outer radius of the cylinder was 4.775 cm, which is the same as the radius of the sphere. The weight of the sphere plus a cylinder of height 0.279 m was 0.129 kg.

Figure 8 shows the large objects.



Figure 8: Large objects submerged in bed. Cylinder with rounded end (left) and sphere (right)

2.2 Determination of the pressure drop through the bed

The pressure drop through the bed was determined by incrementally adding more alumina oxide and measuring the drop from the regulator to the atmosphere. The pressure drop associated with the alumina oxide was of interest as opposed to the pressure drop

associated with the plenum and perforated sheet. In order to determine the pressure drop through the sand, dP/dz , the pressure drop was measured first while there was no sand in the bed with the flow rate set to 24 scfh. This provided the pressure drop associated with the plenum and the perforated plate. Next, the flow was shut off and a volume of sand was added. The flow was turned back on to the same flow rate as before and the pressure drop was measured again. This was repeated until several measurements were recorded. By subtracting out the pressure drop associated with the plenum and the perforated plate from the total pressure, the pressure drop through the sand could be determined. Taking this value and dividing by the bed height yielded dP/dz . The pressure drop through the sand was used to calculate the upwards component of the buoyant force exerted on the sphere.

2.3 Bed height rise associated with submersion of sphere

For the experiments measuring the bed height, the sphere was attached to a Unislide above the bed. The Unislide is an off the shelf product sold by Velmex Inc. It is made of a fixed block marked with a ruler and sliding block. The fixed block has a threaded rod that spans the block's length. Attached to this rod is the sliding block. The threaded rod is attached to a knob that when turned moves the sliding block along the fixed block (refer to Figure 9 for clarity). The displacement of the sliding block can be measured against the ruler marks on the fixed block. In order to tailor the Unislide for the purposes of the present work, another block was added to the sliding block on the Unislide. The attached block had a hole with a set screw. One end of a stake was inserted into the sphere opening and the other end was placed through the hole on the block and tightened with

the set screw, thus fixing it to the Unislide. The Unislide was attached to the fluidized bed by bolting it onto the outer rim of the bed, such that the slide would move vertically up and down into and out of the bed. It was positioned such that the sphere aligned with the center of the bed. Thus, the sphere could be moved along the vertical axis of the bed by turning a knob. The ruler on the Unislide was subdivided into increments of 0.0254 cm. The slide was moved slowly so that the sphere could be held in place at different vertical positions along the bed.

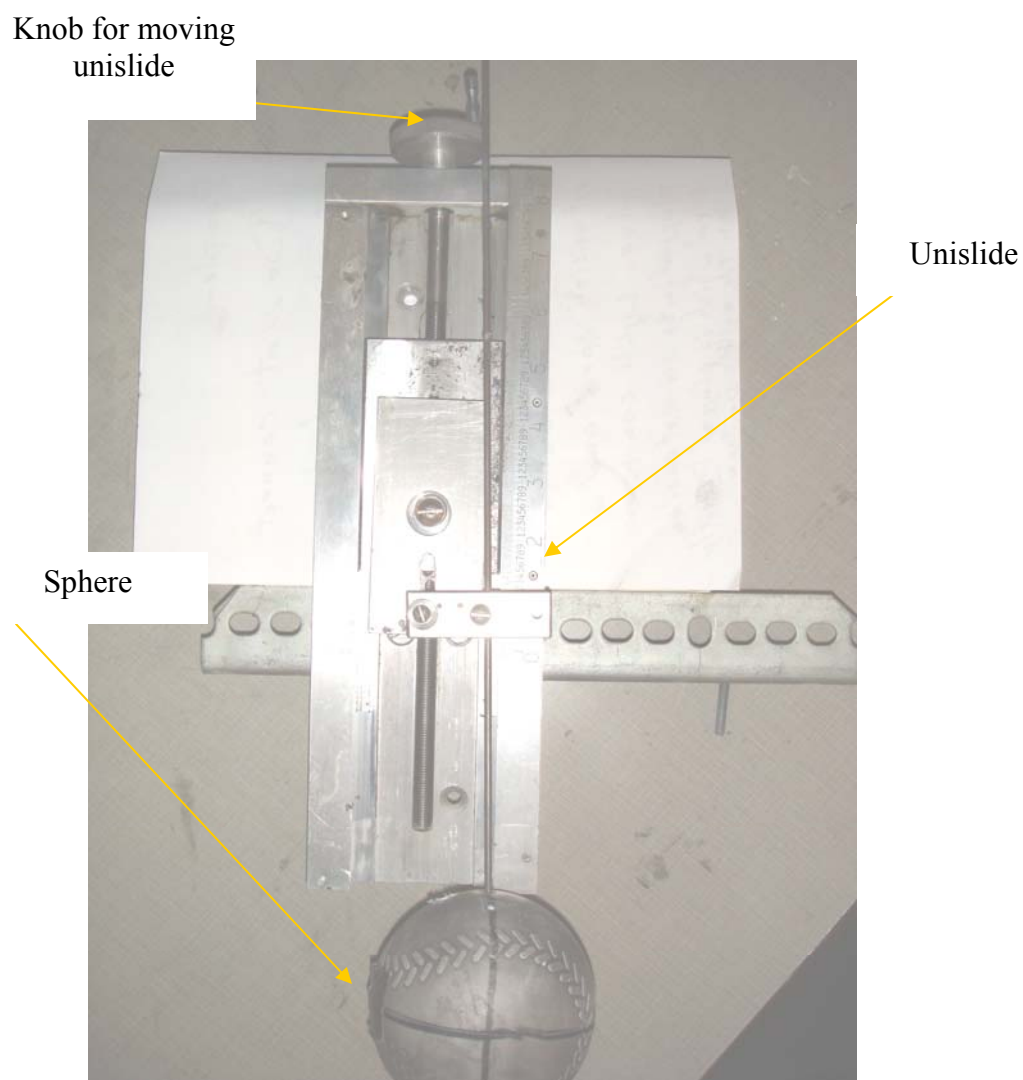


Figure 9: Unislide assembly

A photodiode connected to a PC and analyzed through Labview was used to measure the bed height. The sensor was installed in a plexiglass case measuring 13.5 cm x 4.5 cm x 2.5 cm and connected to a long aluminum threaded rod that could screw into the top of the bed. The diode was placed such that it was partially submerged in the fluidized bath and slightly offset from the wall radially. Voltage potentials could be measured at each end of the diode and a voltage drop could be measured across the diode and outputted in Labview. Figure 10 provides a schematic of the set-up.

The diode was divided into two regions – the top half and the bottom half. Shadows on one end would reduce the potential observed on that same end. A 250 W light bulb was used as a strong light source to increase the amplitudes of the observed voltage drops. The light was installed on a fixture that could also be screwed onto the top of the bed. As the sphere was submerged with the flow rate held constant, the bed would rise in height. The diode was positioned such that the bottom half was always completely submerged and as the bed height rose, the top half would become increasingly covered.

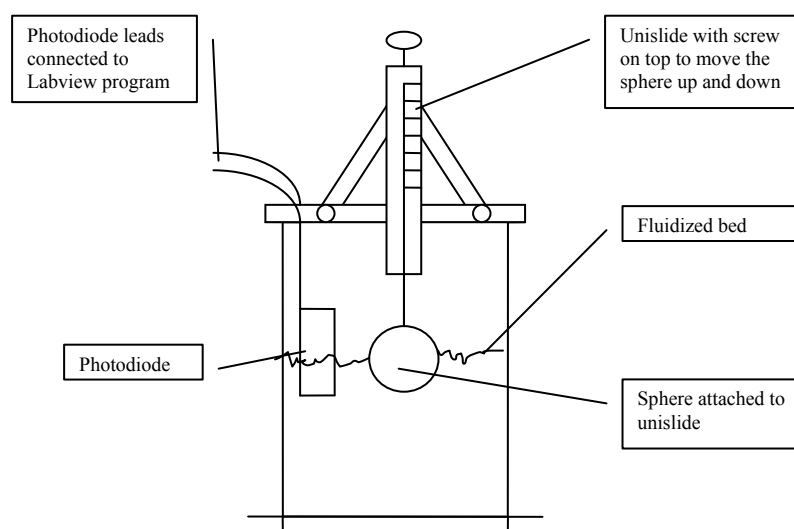


Figure 10: Schematic of set-up for bed height measurement

The diode was essentially a photovoltaic and therefore a decrease in exposed light would decrease the potential on the side that was being covered.

Thus, as more of the diode was covered up, the voltage difference between the two ends would change. Pictures of the set-up can be seen in figures 9 and 10.



Figure 11: Picture of bed height measurement assembly



Figure 120: Top-down view of bed height measurement assembly

In order to convert the voltage difference into a height reading, the diode was calibrated by measuring the bed height with a ruler and comparing it to the voltage difference outputted by Labview. In order for the calibration to be accurate for all measurements, the number of lights on in the laboratory was kept constant, the experiment was kept away from windows and the 250 W light source was located in the same position relative to the diode for all experiments. It was determined that the voltage difference is linearly proportional to an increase in bed height. The results of the calibration are show in Figure 13. For all bed height experiments, the flow rate was kept at 24 scfh.

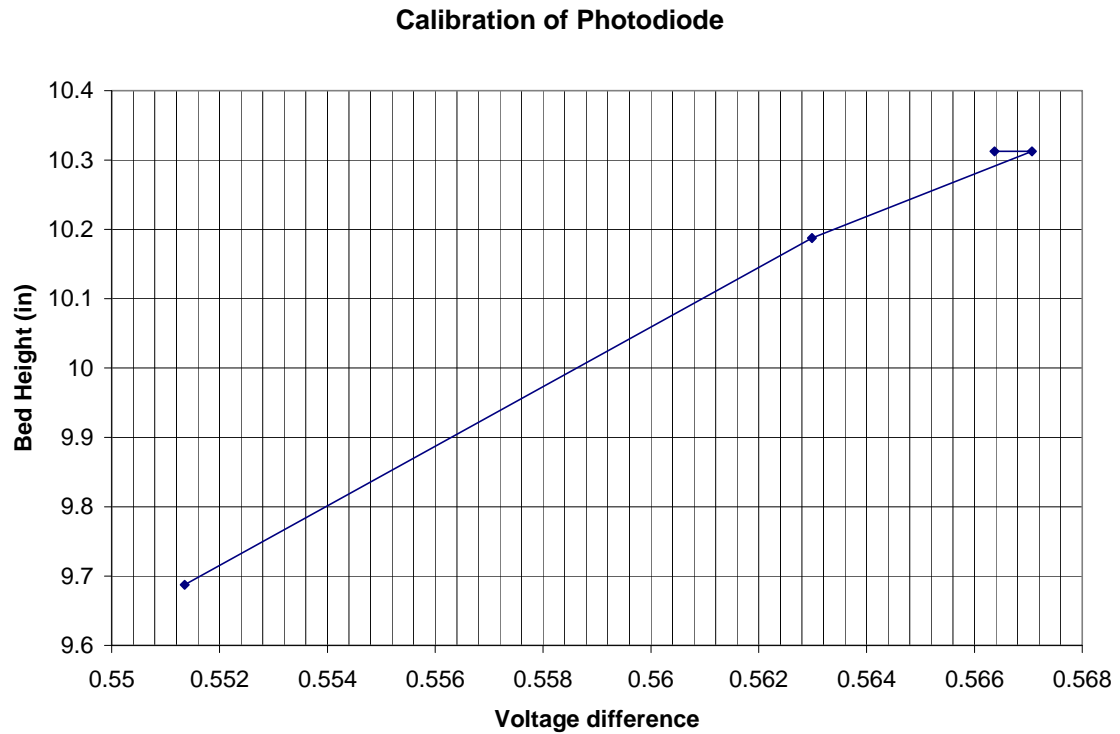


Figure 13: Data for calibration of photodiode

2.4 Forces on Submerged Objects in a Fluidized Bed

For the experiments measuring the forces on the sphere, the sphere was held above the bed by a support beam with two legs. The support essentially straddled the fluidized bed. Either leg of the support was anchored to a base of sand which in turn stood on a weighing scale. The sphere was attached to the support by a threaded rod (size 8-32) staked through the top of the sphere. The other end of the rod was threaded through the support so that when turned, the sphere would move in and out of the bed. The support was placed such that the sphere would be located at the center of the bed. Initially, the sphere was held above the level of the fluidized bed and the scales were zeroed. The sphere was turned 0.4 cm into the bed and the mass as measured on the scales was

recorded. As the sphere was submerged, it would be subjected to the forces within the bed. An increase in the magnitude of the force measured by the scales indicated an increase in the net force on the sphere. Similarly, a decrease in the force on the scale indicated a reduction in the net force. This was repeated and readings were taken until the change in force on the sphere was unchanged with increased penetration. Experiments were run at two flow rates: 40% and 60% of scfh of 40 scfh. This corresponds to $1.26 \times 10^{-4} \text{ m}^3/\text{sec}$ and $1.89 \times 10^{-4} \text{ m}^3/\text{sec}$ respectively. In terms of velocity, this corresponds to $3.5 \times 10^{-3} \text{ m/sec}$ and $5.28 \times 10^{-3} \text{ m/sec}$ respectively. At 40%, the bed was close to the minimum fluidization velocity and therefore this velocity will be referred to as U_{MF} . At 60%, the bed was at the onset of bubbling and will be referred to as $1.5 U_{MF}$ (as it is 1.5 times the minimum fluidization velocity). The stage of fluidization at the flow rates was determined through visual observation.

The same set up was used to measure the forces on the cylinder with a rounded end. However, experiments for the cylinder were only run at $1.5 U_{MF}$.

A schematic of the set up is shown in Figure 14. Pictures of the assembly can be seen in Figures 13 and 14.

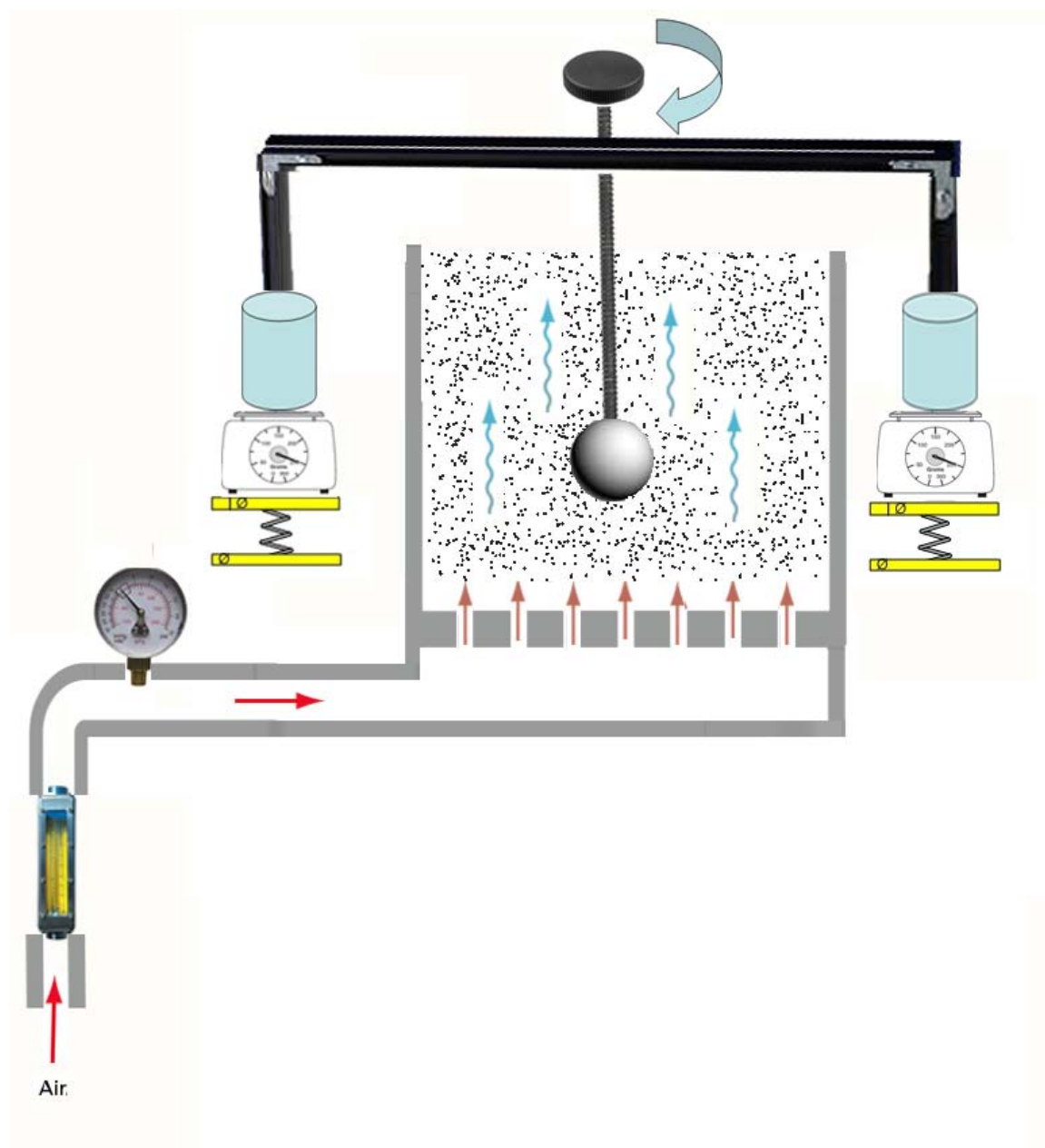


Figure 14: Set-up for experiments measuring forces on submerged objects



Figure 15: Picture of assembly for measuring forces on submerged objects shown outside of bed



Figure 16: Picture of assembly for measuring forces on submerged objects shown inside bed

Chapter 3: Results

The following section will present the results of the experiments.

3.1 Determination of Pressure Drop through the Bed

Using the aforementioned methodology, the pressure drop through the bed was determined. Figure 17 shows the data from the experiments.

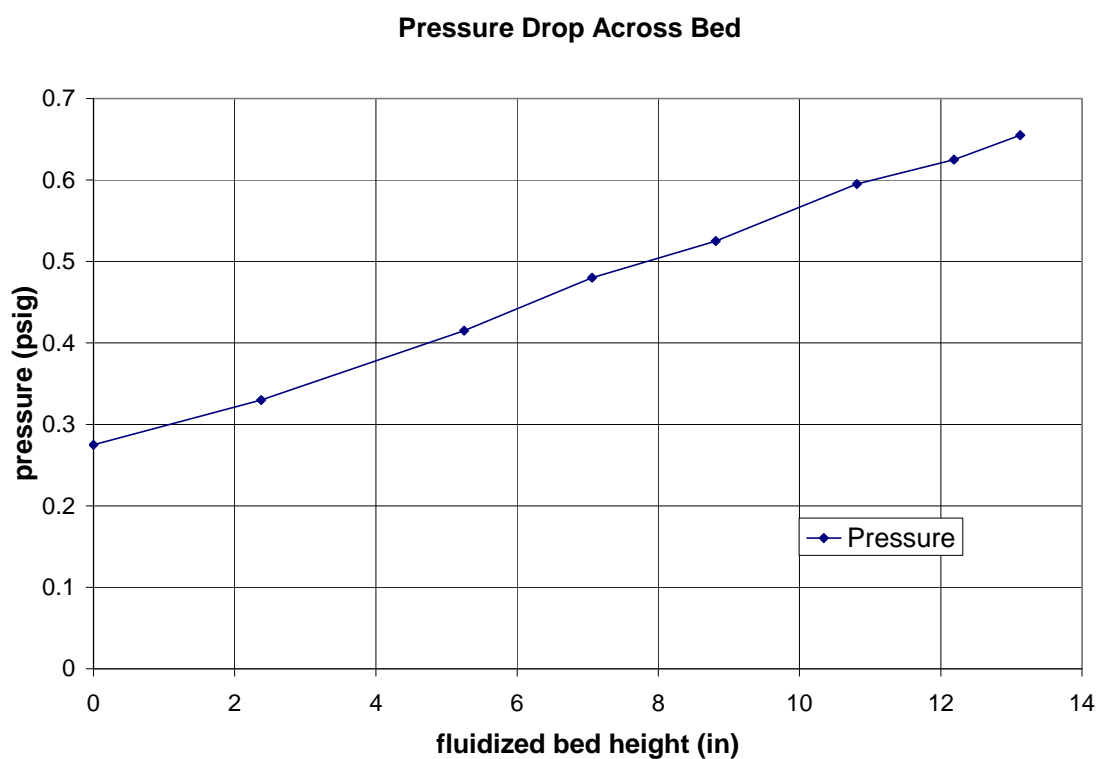


Figure 17: Pressure across bed vs. fluidized bed height

As is clear, the pressure increases linearly as more alumina oxide is added. The equation of the pressure increase with increased bed height obtained from the data is:

$$P_b = 0.0296h + 0.2669$$

Equation 19

Here P_b is the pressure in psig and h is the bed height in inches. The y-intercept of 0.2669 psig corresponds to the pressure drop through the plenum and perforated sheet. The slope of 0.0269 psig/in is the pressure drop associated with the alumina oxide, dP/dz . This value is used in later calculations of buoyancy.

In Howard 1989, it is suggested the drop through the distributor (the plenum and the perforated sheet) should be *at least* 10% of the total pressure drop across the bed for optimal design of a fluidized bed. In the present case, at the fluidized bed height of 10 inches (which is approximately the bed height used in the following experiments), the drop through the distributor is 47% of the total drop across the bed. Therefore, we can verify that the fluidized bed is functioning properly and our pressure drop calculations are reasonable.

3.2 Bed height rise associated with submersion of sphere

Figure 18 shows the measured bed height increase as the sphere was slowly lowered into the bed. The horizontal axis has been scaled to one radius of the sphere, R_{SPHERE} .

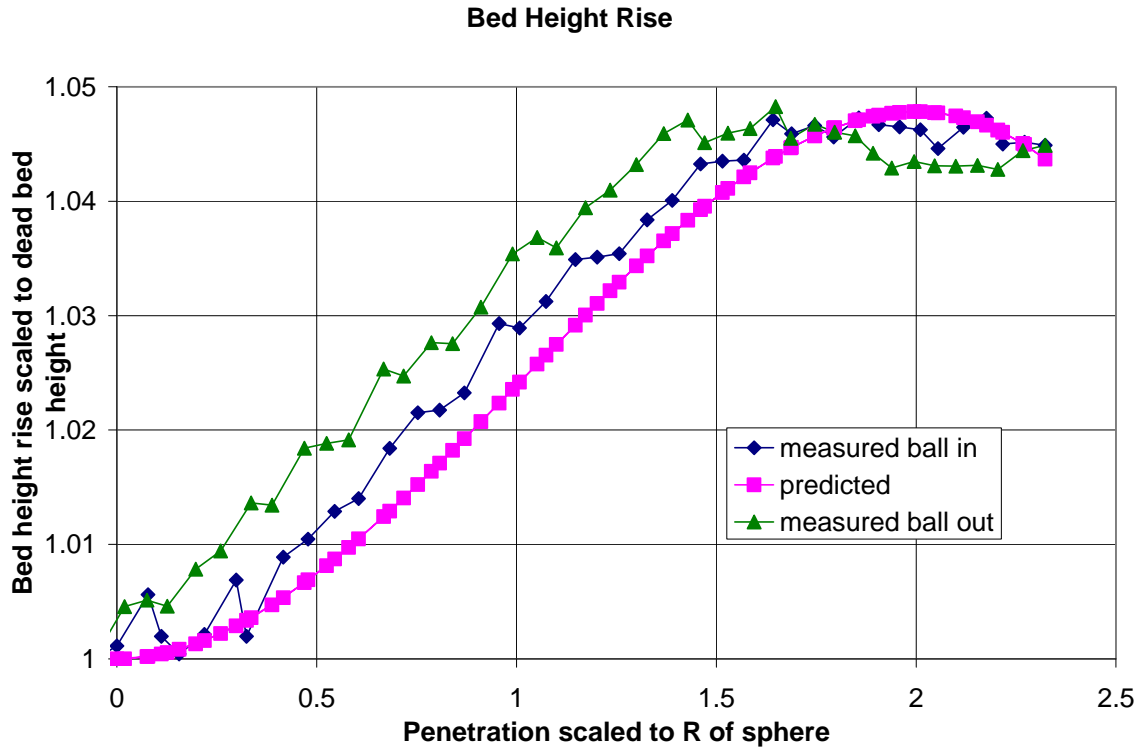


Figure 18: Bed height rise as a sphere is submerged into the bed

The predicted values in Figure 18 were created using a model with the simple assumption that the bed would rise proportionally to the volume displaced by inserting the sphere.

$$\text{Predicted Bed Height} = \frac{\text{Volume of Partially Sunken Sphere}}{\pi R_{FB}^2} + \text{Undisturbed Bed Height}$$

Equation 20

Where,

$$\text{Volume of Partially Sunken Sphere} = \left(\frac{\pi}{3}\right) \times (3R_{SPHERE}h^2 - h^3)$$

Equation 21

In the above, R_{FB} is the radius of the fluidized bed, while R_{SPHERE} is the radius of the sphere and h is the depth that the sphere has sunk. The impact of the de-fluidized hood on the bed height has not been included in the model.

For all bed height experiments, the flow rate was kept constant and at the onset of bubbling (determined by visual observation). The data matches fairly well until the sphere sinks to around a height of $1.75 R_{SPHERE}$. At this point, the model continues to grow, while the data starts to flatten. The de-fluidized region has sufficiently developed such that there is a portion of the bed now dead. This can be visually observed because a dead region on the surface of the fluidized bed above the sphere is apparent. This dead bed portion leads to a less than predicted bed height. For times when the sphere is submerged less than $h = 1.75 R_{SPHERE}$, the bed height is slightly greater than the predicted bed height. However, this under prediction is less than 1% of the total bed height on average. From this, the conclusion can be made that the de-fluidized hood does not begin at a penetration depth greater than $h = 1.75 R_{SPHERE}$. Physically, it cannot begin before $h = R_{SPHERE}$.

Hysteresis occurs as the sphere is pulled out of the fluidized bed. At every point, the bed height is higher – indicating higher levels of fluidization – while the sphere is being pulled out than it is while being pushed in. However, this difference is very small. Even still, hysteresis can be seen when fluidizing and de-fluidizing the bed. The case with the sphere entering the bed can be considered de-fluidization because a portion of the bed is being deadened whereas the bed is fluidized as the sphere is removed from the bed.

because the deadened region created by the sphere is now being re-fluidized. Figure 19 taken from data presented by Jackson (2000) shows hysteresis when a bed is fluidized and then de-fluidized. Arrows show the direction of bed height increase. As can be seen, the bed height is higher when de-fluidizing than it is when fluidizing.

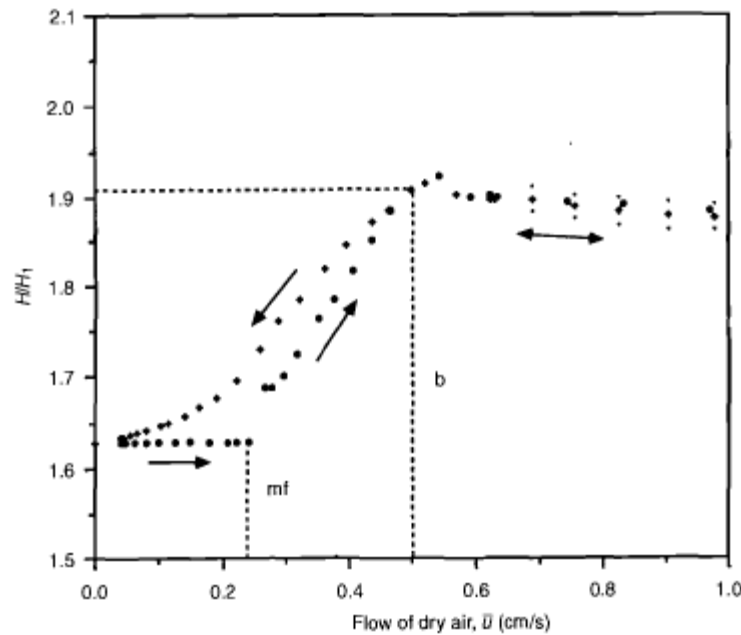


Figure 19: Bed height change during fluidization (right pointing arrows) and de-fluidization (left pointing arrows)

Visual observation of the sphere entering into the bed shows that once the sphere was submerged half way, bubbles would form around the circumference of the sphere. Once the sphere was submerged deeper than R_{SPHERE} , the bubbles would still appear at the surface of the bed. They would form a ring at the surface whose radius would grow as the sphere was lowered deeper. The bubbles would also grow in size as the sphere was lowered.

Figure 18 is a top view drawing of the bubbling ring around the sphere:

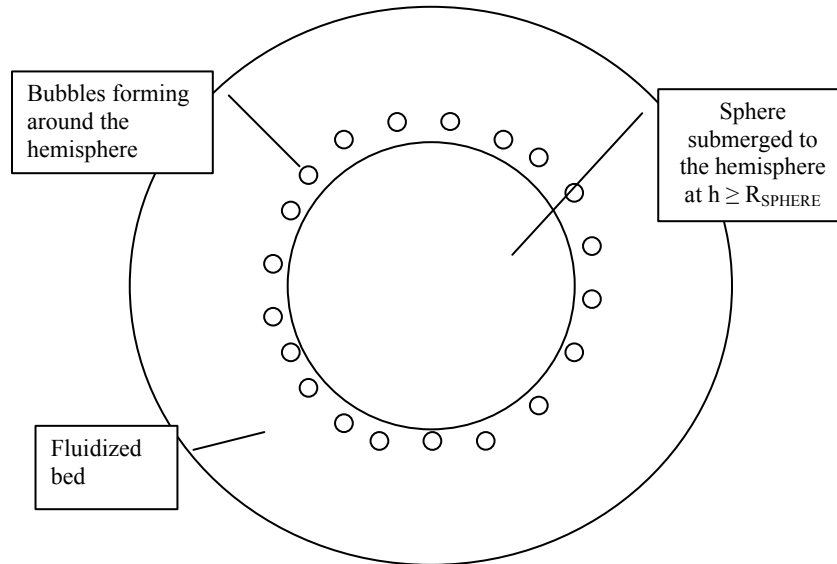


Figure 20: Bubble formation around hemisphere of half submerged sphere

These bubbles are the result of the flow having to accelerate around the sphere at the hemisphere in order to maintain a mass balance for air. Since the bed is already fluidized, air in excess of that needed for fluidization would escape as bubbles. This caused the formation of the ring of bubbles around the hemisphere. The bubbles also visually verify another key phenomenon. If the flow did not separate from the sphere, as it would under Stokes Flow, then the ring of bubbles would not have been observed. However, the presence of bubbles indicates that the flow separates from the sphere at the hemisphere. Therefore, the region above the sphere will have no flow, and this region would be de-fluidized. Consequently, using Stokes's Law for any predictive calculation concerning the de-fluidized hood should be broached with caution. Rees et al (2004) calculated the Reynolds number for their experiment and found it to be less than 1. Thus, the usage of

Stokes's Law was said to be appropriate. However, visual observations of the sphere sinking would seem to indicate that while the sphere may obey Stokes's Law mathematically, in reality, it may not obey it physically.

3.3 Forces on an object submerged in a fluidized bed:

Figure 19 compares the forces on a sphere in a fluidized bed at two different flow rates with the forces on a cylinder sticking out of the fluidized bed with a rounded leading edge. The submerged sphere is subject to form drag, skin drag, buoyancy and the weight of the de-fluidized region, while the submerged cylinder is only subject to form drag, skin drag and buoyancy. A cylinder sticking out of the fluidized bed cannot develop a de-fluidized region. Experiments with spheres at different flow rates were used in an attempt to alter the drag on the sphere.

For $h = 0$ to $h = R_{\text{SPHERE}}$, the cylinder and the sphere at $1.5 U_{mf}$ should be in agreement because the geometries and operating conditions are essentially the same. Thus the drag and the buoyant forces should be the same for the two objects.

From $h = R_{\text{SPHERE}}$ to $h = 2R_{\text{SPHERE}}$, the sphere experiences less growth in total forces than the cylinder. This should be expected as the cylinder has more exposed surface area beyond $h = R_{\text{SPHERE}}$ than the sphere and thus will have a larger drag force.

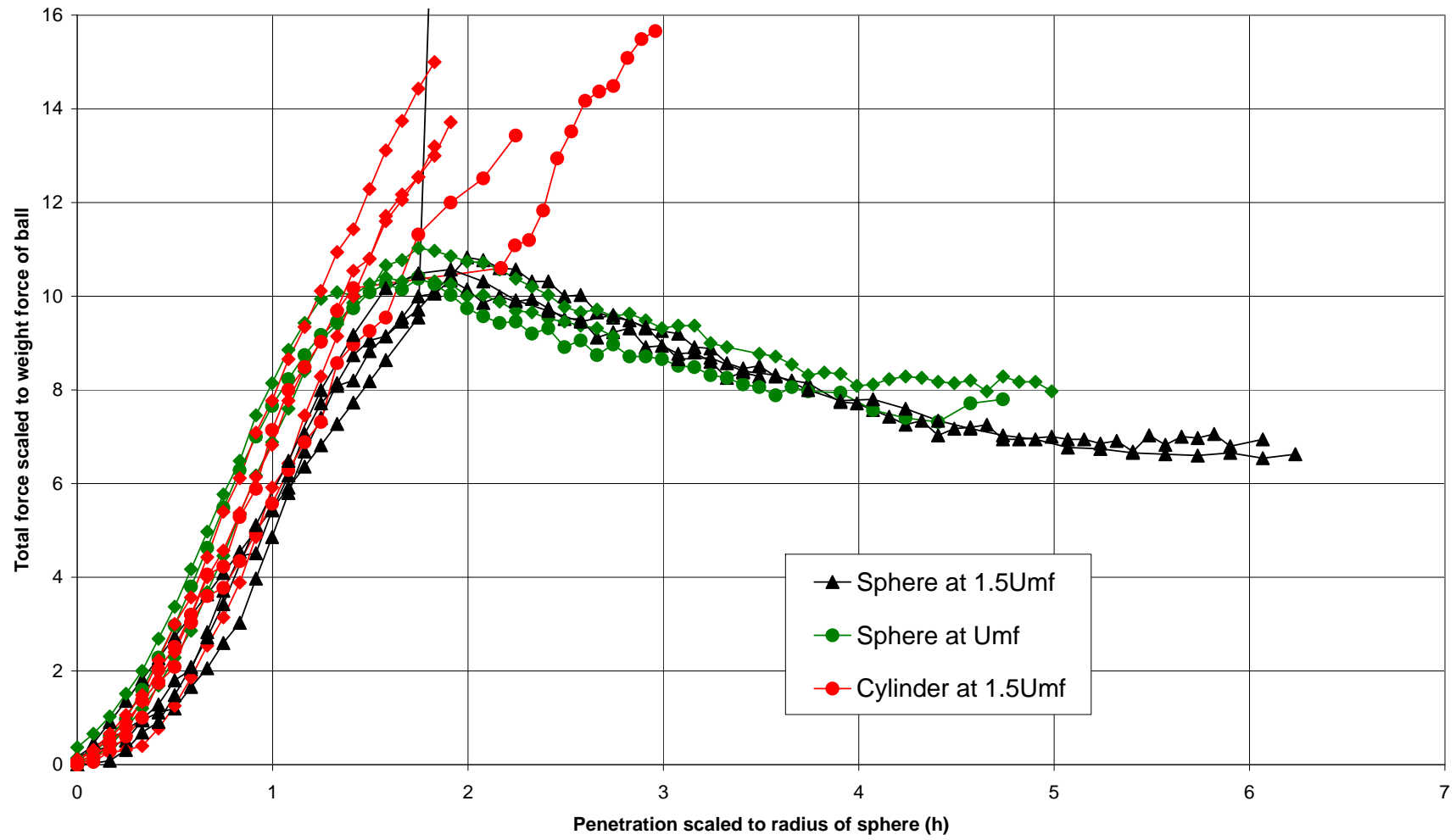


Figure 21: Force on sphere and cylinder in fluidized bed

Once the cylindrical section starts to submerge at $h = R_{\text{SPHERE}}$, the pressure force acting normal and upwards on the body increases linearly with penetration depth. Therefore, the buoyant force should grow at a constant rate with increased penetration. The linearity of the forces on the cylinder beyond $h = R_{\text{SPHERE}}$ indicates that no additional forces, such as a de-fluidized region, are created.

The total forces on the sphere begin to reduce at $h = 1.8R_{\text{SPHERE}}$. This can be attributed to the creation of the de-fluidized hood. This assertion is made because a sphere without a de-fluidized section would experience no additional forces after it was completely submerged (i.e. the forces for the sphere in Figure 21 would flatten out past $h = 2R_{\text{SPHERE}}$). In the current case, the force on the sphere begins to decrease once the sphere is nearly submerged. Therefore, an additional downward force is now observed. After a certain point ($h = 4.41R_{\text{SPHERE}}$ for $1.5 U_{\text{mf}}$ flow and $h = 4R_{\text{SPHERE}}$ for U_{mf} flow) the forces in Figure 21 flatten out. At this point, it is hypothesized that the de-fluidized region is at its maximum size.

A comparison between the sphere under U_{mf} flow and $1.5U_{\text{mf}}$ flow for h between 0 and $2R_{\text{SPHERE}}$ yields the result that the sphere under U_{mf} flow is subjected to larger forces. Although the flow rate is lower, the density is higher. The increase in density is due to the decrease in fluidization caused by the lower flow rate. The denser phase leads to more collisions between the particle and the sphere. This would lead to an increase in viscosity. The increase in viscosity with lower flow rates has been reported in the literature (Liu

1960, Davidson 1977). The buoyant force for the U_{MF} case will also be increased since the density increase will yield a greater pressure drop through the sand.

Chapter 4 Theoretical Model

An attempt to derive the force balance on the sphere can now be made and its accuracy can be verified using the data. A model was developed for comparison to the data of the sphere at $1.5 U_{MF}$.

The forces on the sphere are as follows, with h being the depth to which the sphere has penetrated the bed surface:

$$\begin{cases} \text{Form Drag + Skin Drag + Buoyant Force,} & 0 < h \leq R_{\text{SPHERE}} \\ \text{Buoyant Force + De - Fluidized Hood} & h > R_{\text{SPHERE}} \end{cases}$$

4.1 Determination of Form Drag

Visual observation indicated that form drag would not be a major contributor to the force on the sphere. In an empty bed, at the flow rate used in the aforementioned experiments, the sphere would not move at all, thus indicating a small form drag force.

The form drag was determined through a momentum balance around the sphere. The velocity around the sphere penetrating a distance h into the bed was determined using Equation 22.

$$U_1 = U \frac{A}{A_2 \varepsilon}$$

Equation 22

Where:

$$U = \frac{\dot{V}}{A}$$

$$A = \pi R_{FB}^2$$

$$A_1 = A - \pi \left(\frac{D_{wetted}}{2} \right)^2$$

$$\varepsilon = \frac{Ah_{pred} - \pi \left(R_{FB}^2 h^2 - \frac{h^3}{3} \right)}{Ah_{pred}}$$

And

$$D_{wetted} = 2\sqrt{2R_{SPHERE}h - h^2}$$

Equation 23

Here, U is the fluidization velocity, \dot{V} is the volumetric flow rate as measured on the rotameter and A is the cross sectional area of the bed. R_{FB} is the radius of the bed, A_1 is the area of bed around the sphere at a particular penetration height, h , measured as being the depth at which the bottom of the sphere has been submerged into the bed, D_{wetted} is the wetted diameter of the sphere at the penetration height, measured as being the chord length across the sphere at this penetration. ε is the bed voidage, or percent of the bed that is air, and h_{pred} is the predicted bed height.

In order to calculate the momentum difference around the sphere, the bed density, ρ_f , needs to be determined. Equation 24 was used for this purpose

$$\rho_f = \frac{M_{sand}}{V_{bed}}$$

Equation 24

M_{sand} is the mass of alumina oxide in the bed and V_{bed} is the volume of the fluidized bed using the predicted bed height.

By calculating the momentum deficit at a position along the sphere up to R_{SPHERE} , we can find the form drag along the sphere.

$$\text{Form Drag} = \rho_f (U^2 A - U_1^2 A_1)$$

Equation 25

For the experiments, the form drag was on the order of 10^{-2} N or 0.06 times the weight of the sphere.

Figure 22 shows the form drag variation with penetration depth:

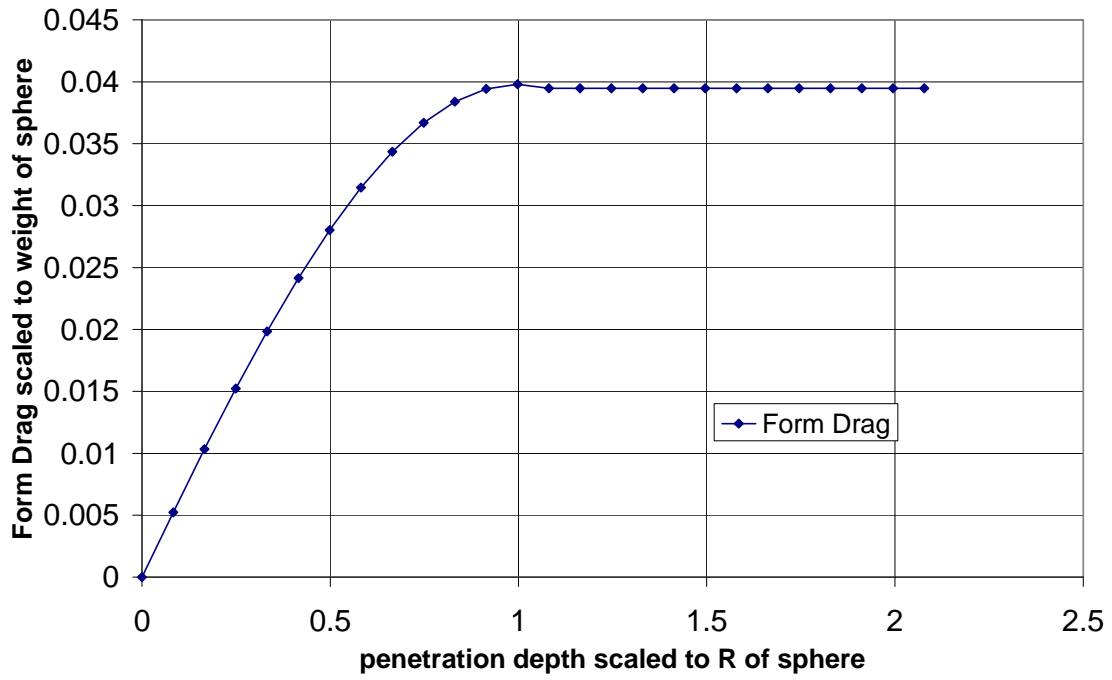


Figure 22: Form drag on a submerged sphere

Past $h = R_{\text{SPHERE}}$, the form drag remains constant since the air flow is no longer impacting the sphere.

4.2 Determination of Buoyant Force

In a static fluid, the buoyant force is calculated using Archimedes Principle:

$$\frac{dP}{dz} = \rho_f g$$

Equation 26

The buoyant force is an effect of the pressure difference above and below the immersed object. By integrating the pressure over the surface of the immersed object, the buoyant force is attained for a submerged object in a static fluid.

From Equation 19, dP/dz , the pressure drop associated with the alumina oxide, is:

$$\begin{aligned}\frac{dP}{dz} &= 0.0296 \text{ psi/in} \\ &= 7926 \text{ Pa/m}\end{aligned}$$

Now, calculating dP/dz through Archimedes Principle, using the density calculated in Equation 24 of 843.4551 kg/m^3 , gives 8265.86 Pa/m (Equation 26). These two solutions are within 4% of each other. The similarity in the two results gives confidence that pressure drop observed is accurate.

Integrating dP/dz over the sphere yields the buoyant force on a sphere without a de-fluidized hood:

$$Force_{buoyant} = \int_0^{2\pi} \int_0^{\pi} \int_0^h \left(\frac{dP}{dz}\right) R_{\text{sphere}}^2 \sin(\theta) dz d\phi d\theta$$

Equation 27

Where

$$\frac{dP}{dz} = \rho_f g = 7926 \text{ Pa/m}$$

The pressure force will act normal to the surface of the object. Only the vertical component (along the axis of the bed) of the force is of interest as the hood will act purely vertically and the forces measured were all vertical. In order to obtain the vertical component of the pressure force, Equation 27 is multiplied by $\cos(\theta)$, where θ is the angle swept from the bottom of the sphere to the bed surface. This can be expressed as:

$$\theta = \tan^{-1}\left(\frac{\frac{d_{wetted}}{2}}{R - h}\right)$$

Equation 28

In the case of an object with a de-fluidized hood, the pressure force acting downward for $h > R_{\text{sphere}}$ is difficult to attain through integration around the surface for a variety of reasons. One such reason is that once the hood forms, the pressure drop felt by the top of the sphere will be different than that felt by the bottom of the sphere because the region above the sphere is not fluidized. Therefore, the dP/dz measured for the fluidized bed is no longer valid for the upper half of the sphere. A similar argument would be that Archimedes Principle assumes that the density of the fluid is uniform all around the submerged object. In the case of objects with de-fluidized hoods, the density around the object is different at the top and the bottom. The earliest the hood could begin is at $h = R_{\text{SPHERE}}$. Therefore, since the object under investigation has a de-fluidized hood, the integration to calculate pressure force shown in Equation 27 was only calculated for $0 \leq h \leq R_{\text{SPHERE}}$. The result is the pressure force acting up on the bottom half of a submerged object. As the object gets submerged deeper, this force increases because the pressure increases with depth. The results are shown in Figure 23. The downward component of

the pressure force on the sphere will be determined by calculating the de-fluidized hood weight in section 4.4.

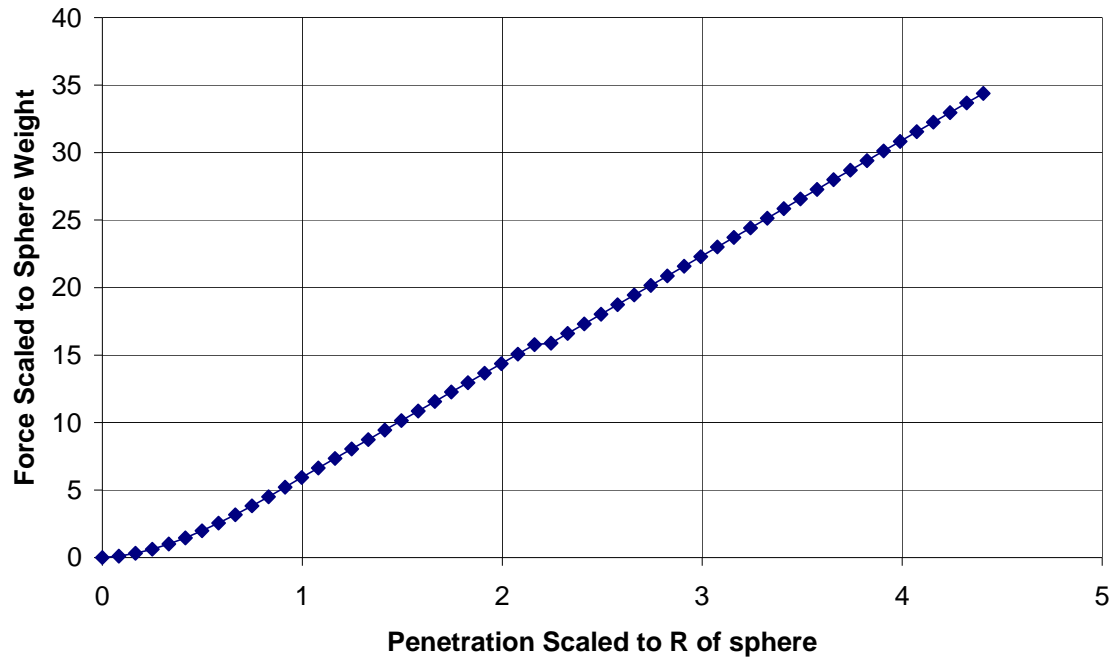


Figure 23: Pressure Force Pushing Submerged Object Up and Out of Bed

Figure 23 also predicts the buoyant force on the cylinder since the cylinder is never fully submerged and does not have a de-fluidized hood. In the case of the sphere, Figure 23 only predicts the upward component of the buoyant force.

4.3 Skin Friction Determination

Although the apparent viscosity has been estimated to be approximately 1 kg/m-sec by previous researchers, calculating the skin friction on the sphere was still not obvious. Past researchers have determined that the flow within fluidized beds can be modeled as Stokes' Flow and thus Stokes' drag is applicable. However, in the present case, through

visual observation, it is clear that the flow separates from the sphere and is thus not typical Stokes' flow. The visual observations that led to this conclusion include:

- 1) The existence of the hood requires that there is no flow above the sphere, thus allowing de-fluidization.
- 2) Bubbles around the hemisphere of the sphere are observed, thus indicating a flow separation

In the present work, use of an alternate method of determining skin friction was necessary.

The forces in the case of the cylinder are as follows:

$$\begin{cases} \text{Form Drag} + \text{Skin Drag} + \text{Buoyant Force}, & 0 < h < R_{\text{SPHERE}} \\ \text{Skin Drag} + \text{Buoyant Force}, & h > R_{\text{SPHERE}} \end{cases}$$

With the buoyant force on the cylinder determined, the experimental forces on the cylinder can be used to determine a drag coefficient. This coefficient can then be applied to the case of the sphere.

The common equation for drag force where it is related to the momentum of the flow is used:

$$F_{Drag} = \frac{1}{2} \rho_f U^2 A_{wetted} C_D$$

Equation 29

Where

$$A_{wetted} = \int_0^h 2\pi R_{SPHERE}^2 (1 - \cos \theta) dz = 2\pi R^2 \left(\frac{h}{R}\right)$$

$$\theta = \sin^{-1} \left(\frac{d_{wetted}/2}{R_{SPHERE}} \right)$$

Equation 30

Since the buoyant force and form drag on the cylinder have been determined, these can be subtracted out from the experimental data of the forces on the cylinder. Doing so would reduce the data to the skin drag along the cylinder.

Before applying Equation 29, an adjustment is made to the velocity around the cylinder. The only velocity of interest when calculating the skin drag is the velocity tangential to the object. Thus, to find the velocity of interest, U_T , the following is employed with U_1 and θ from before:

$$U_T = U_1 \cos\left[\left(\frac{\pi}{2} - \theta\right)\right]$$

Equation 31

This now gives the velocity tangential to the surface of the submerged objects, and thus the velocity associated with skin drag. Using Equation 29 in Equation 29Equation 31 and comparing to the data will give a value for the drag coefficient.

The experimental force less the buoyant force and the form drag for the cylinder is graphed in Figure 24 (shown as “experimental skin friction”). The experimental data shows variation. However, the variation is negligible when compared to the total forces on the cylinder.

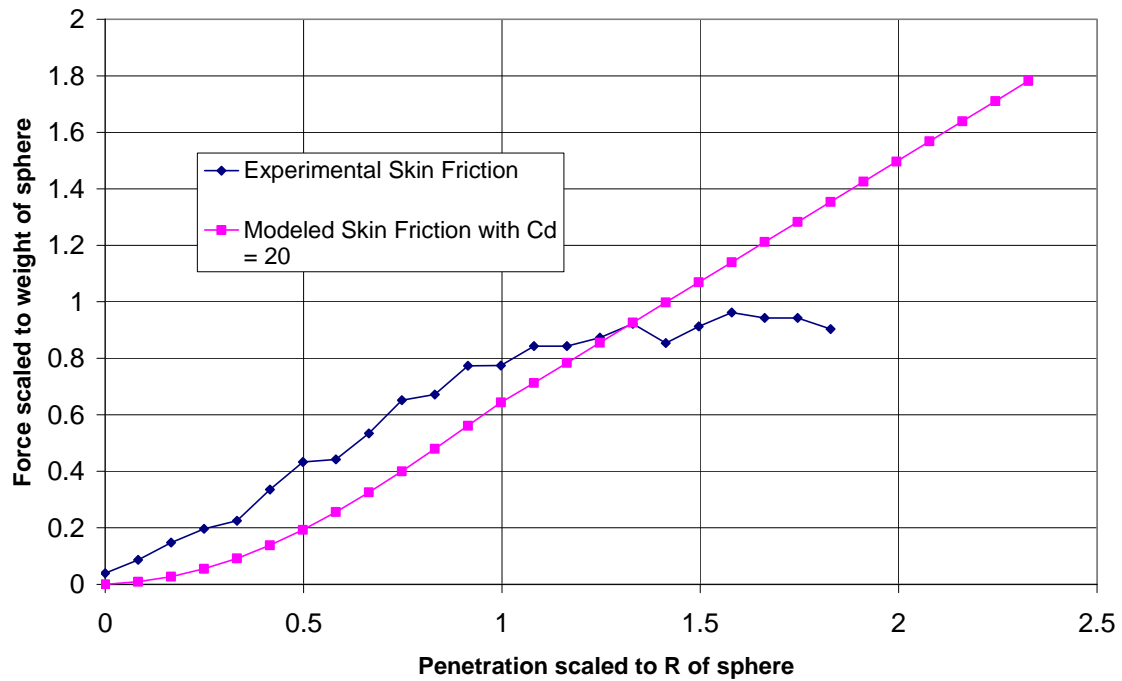


Figure 24: Skin friction on cylinder compared to theoretical skin friction with $C_d = 20$ in equation 29

Using a drag coefficient of 20 in Equation 29, the data and the model for the cylinder are compared in Figure 22. There is good agreement between the two. Figure 25 shows the total experimental force on the cylinder compared to the model. The model is the sum of the predicted form drag, buoyant force and skin drag

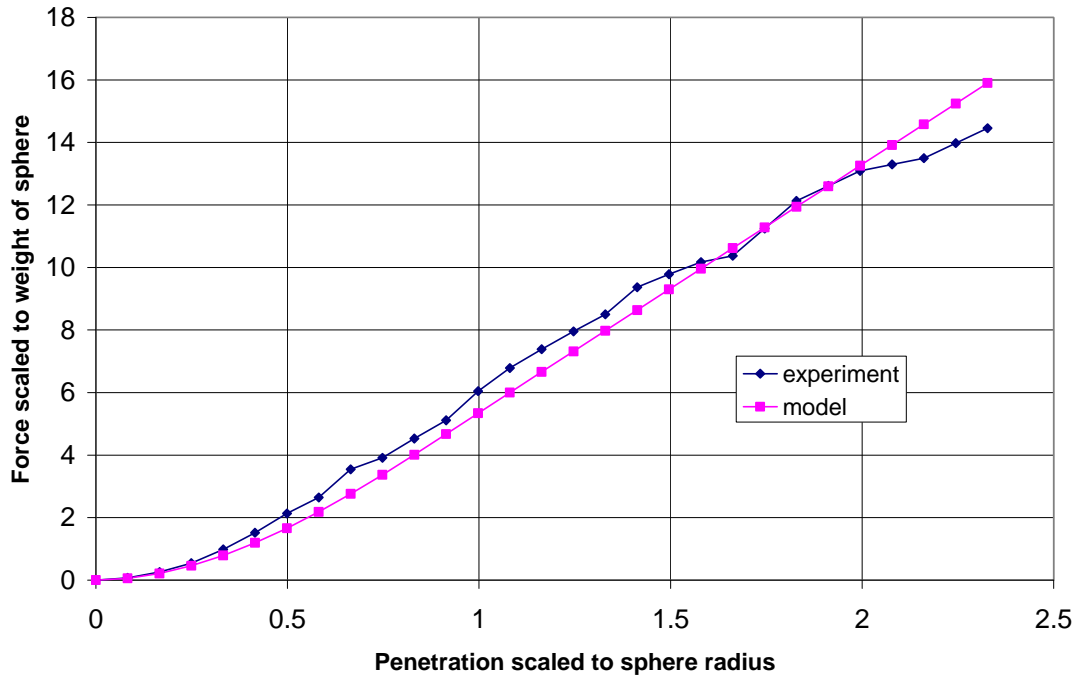


Figure 25: Predicted force on cylinder compared to experimental force

Now, assuming the drag coefficient for the sphere and cylinder are the same, the skin drag on the sphere is readily attainable through use of Equation 29. For regions past $h = R_{\text{SPHERE}}$, the flow is considered to have separated from the sphere. Therefore, the skin drag will no longer grow.

Using the velocity in Equation 31 in Equation 29, Figure 26 for the skin friction on the sphere is obtained.

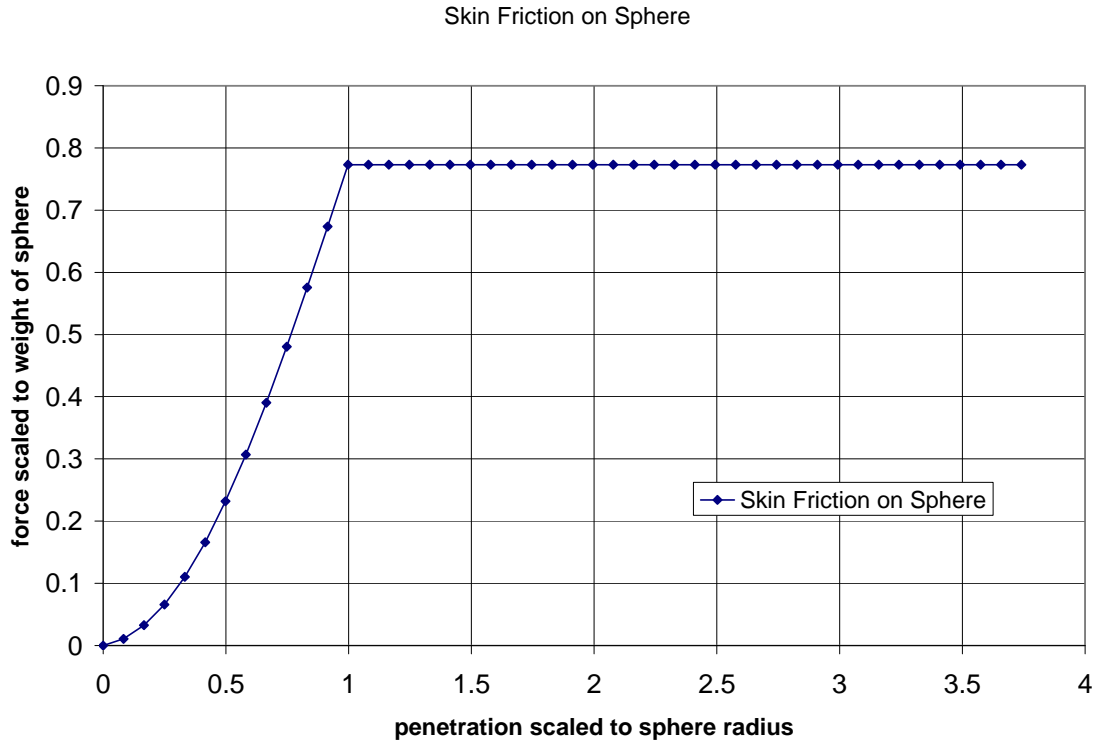


Figure 26: Prediction of skin friction on sphere at 1.5U_{mf} flow

In order to compare to the relations proposed by Crowe et al (Equation 12 and Equation 13) it is necessary to determine f (the friction factor) and the Reynolds number, Re . The Reynolds number can be calculated using Equation 32 where ρ_f is the density of the fluidized bed (calculated from Equation 24), U_1 is the velocity around the sphere (Equation 31), d_{sphere} is the diameter of the sphere and μ_{bed} is the viscosity of the fluidized bed (taken to be 1 kg/m-sec as recommended by Davidson 1977).

$$Re = \frac{\rho_f U_1 d_{\text{sphere}}}{\mu_{\text{bed}}}$$

Equation 32

With the calculated values of Re , obtained by making the assumption that the particle motion with respect to the interstitial gas velocity is negligible, the friction factor is determined using **Error! Reference source not found.** This will determine the drag coefficient according to Equation 12. Using the velocity corresponding to when the sphere is submerged up to the hemisphere, an Re of 4.26 and a drag coefficient of 7.9 is obtained. Our drag coefficient of 20 based on the data from the cylinder is ~ 2.5 times the value predicted by the literature. However, the value used in the literature is based on an order of magnitude estimate of the viscosity being 1 kg/m-sec.

4.4 Determination of De-fluidized Hood Weight and Shape

The final force on the sphere is that created by the de-fluidized hood. From Figure 18, it is apparent that this region begins no later than at $h = 1.75R_{\text{SPHERE}}$. Also, intuitively, it can occur no earlier than at $h = R_{\text{SPHERE}}$. For regions at $h < R_{\text{SPHERE}}$, the hood has no place to grow.

In order to obtain a hood weight and shape, the experimental data over several runs was averaged and a 10th degree polynomial curve was fit to the data. Using a trend line rather than directly using the experimental data smoothed out any variations in the data caused by voids or by the act of lowering the sphere deeper into the bed. Both of these would disturb the hood, knocking it down and lowering its size for a short while until the hood is rebuilt. Using the DataFit software, the following trend line was fit to the sphere at $1.5 U_{\text{MF}}$:

$$F_{\text{TOTAL}} = (1.91 \times 10^{-4})x^{10} + (-4.28 \times 10^{-3})x^9 + (3.46 \times 10^{-2})x^8 + (-8.29 \times 10^{-2})x^7 + (-0.462)x^6 + (3.76)x^5 + (-10.58)x^4 + (13.25)x^3 + (-5.97)x^2 + (1.76)x + (1.91 \times 10^{-4})x^{10} - 5.08 \times 10^{-3}$$

Equation 33

Figure 27 shows the average data compared to the trend line for the sphere at $1.5 U_{MF}$.

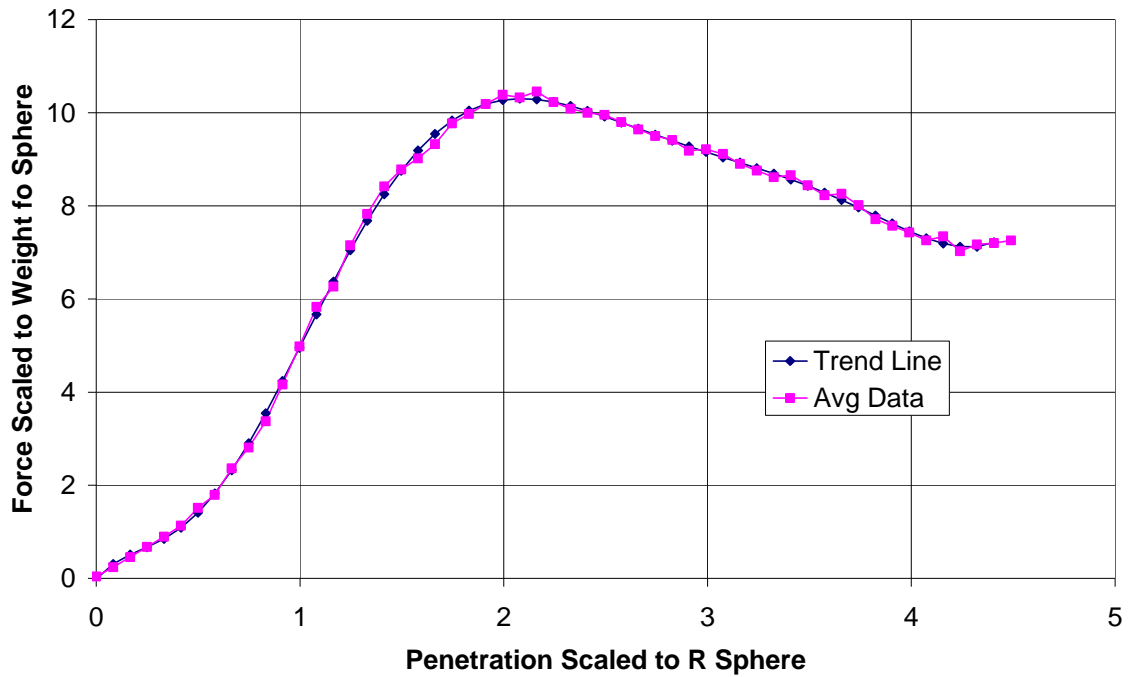


Figure 27: 10th degree polynomial trend line fit to average data for 1.5 Umf sphere

The pressure force, the skin drag and the form drag were all assumed to be applicable up until $h = R_{\text{SPHERE}}$. Beyond this point, the overall shape of the submerged object (the sphere plus the hood) is undeterminable since the hood may begin to grow as early as $h = R_{\text{SPHERE}}$. It will be assumed that the only additional force acting on the upper half of the

sphere is that of the pressure force exerted by the dead bed region above the sphere. With this assumption, the following relation can be developed:

$$F_{ABOVE} = \rho_{hood} g V_{hood} = F_{EXPERIMENTAL} - F_{PRESSUREUP} - F_{SKINDRAG} - F_{FORMDRAG}$$

Equation 34

Essentially, the hood force is the remaining force after the upwards pressure force, skin drag, and form drag are subtracted out from the experimental data.

F_{ABOVE} from Equation 34 is graphed in Figure 28

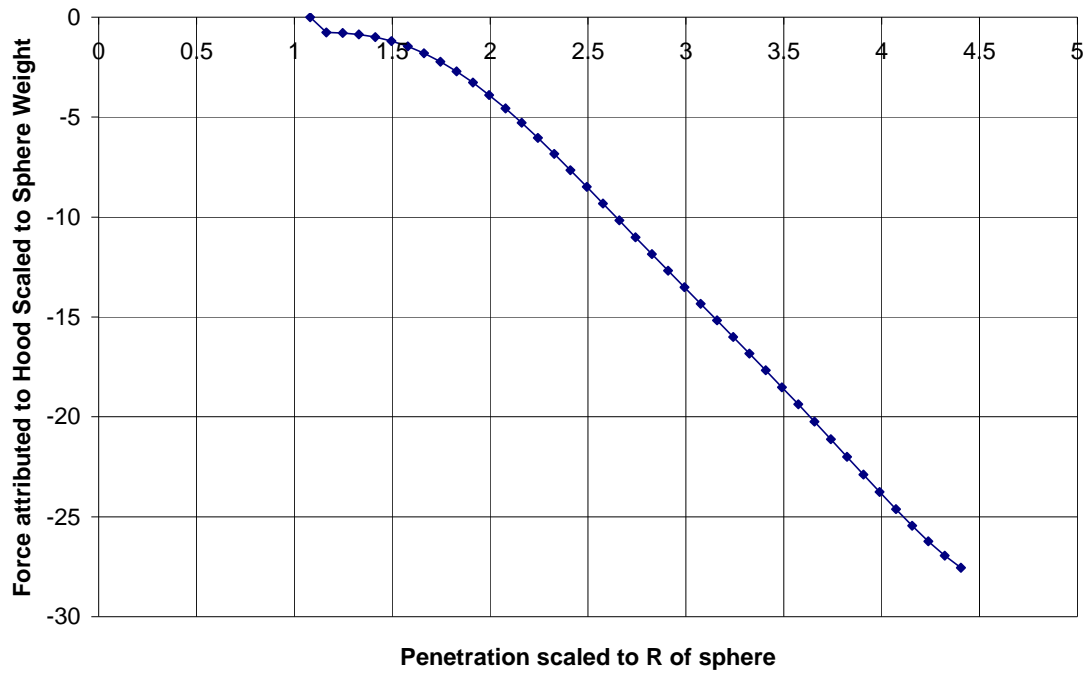


Figure 28: Force from above on sphere

As can be seen, F_{ABOVE} is negative, indicating that the de-fluidized hood force acts to push the sphere deeper into the bed.

In order to determine the shape of the hood, it can be assumed that the hood is comprised of small cylinders with height dh stacked upon each other. The radius of each cylinder would be dependent on the incremental increase in hood weight over a height, dh . Applying this to Equation 34, the following equation is obtained:

$$dF_{ABOVE} = \rho_{hood} g \pi (r_{cylinder})^2 dh = d(F_{EXPERIMENTAL} - F_{PRESSUREUP} - F_{SKINDRAG} - F_{FORMDRAG})$$

Equation 35

The density of the hood was taken to be that of the alumina oxide. In taking this to be the density, it has been assumed that hood consists of completely un-fluidized alumina oxide. By using Equation 35, the radius of each cylindrical element can be determined. With the dimensions of each cylindrical section now known, the de-fluidized hood shape can be determined. The results for the hood shape are shown in Figure 29. The hood has been superimposed over the submerged sphere. The dashed line indicates the portion of the sphere covered by the de-fluidized hood. For the most part, the hood resembles a cylinder with a short and rounded top.

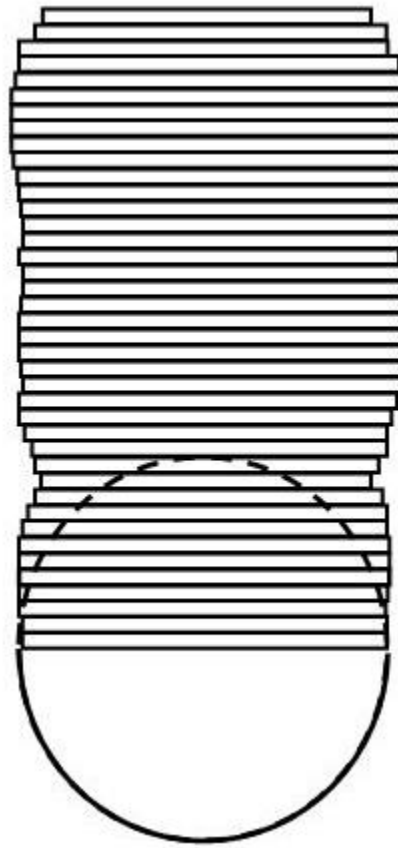


Figure 29: Hood Shape Extracted from Hood Weight Data

The maximum hood height was also studied. Experimentally, the data shows that the hood ceases to grow at $h = 4.41R_{\text{SPHERE}}$ for the $1.5U_{\text{MF}}$ case, or a hood height of $3.41R_{\text{SPHERE}}$ (calculated from the center of the sphere). This hood height is 1.71 times the diameter of the submerged sphere.

4.5 Summation of Model Forces

The summation of the models for form drag, buoyancy, skin drag and the hood weight are shown in comparison to the experimental results for the sphere at 1.5 Umf in Figure 30.

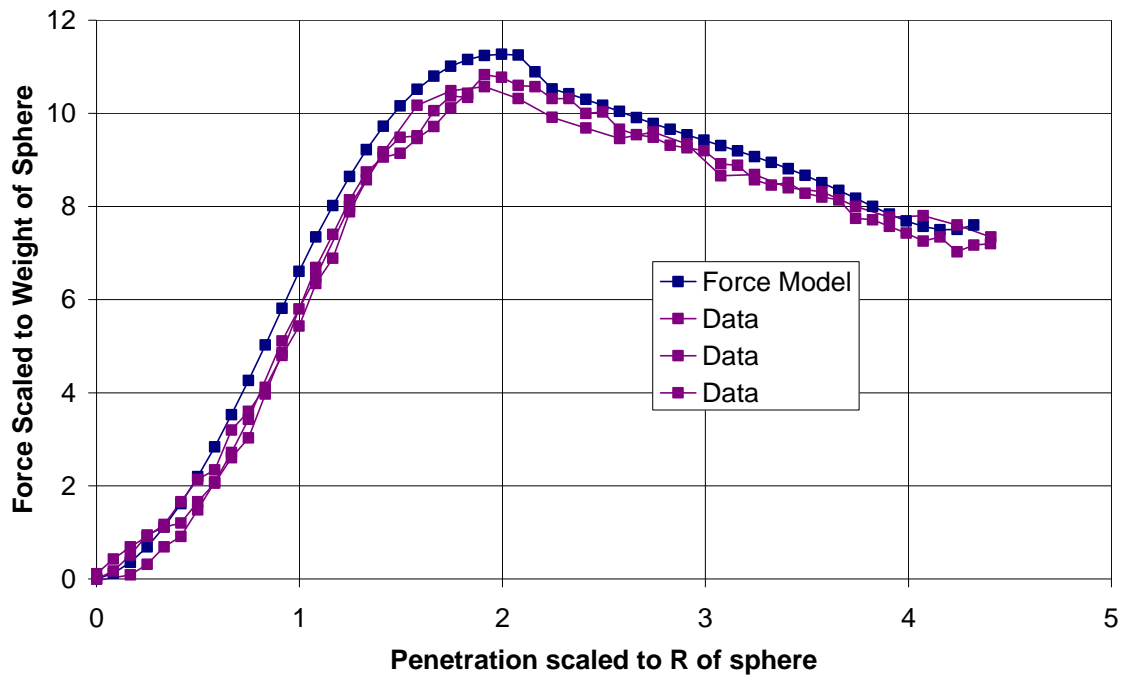


Figure 30: Comparison of model to data for 1.5 Umf flow sphere case

The model fits the data well. While the model shows the force as being slightly higher than the data values, the variation is at most 7% (occurring at $1.8R_{\text{SPHERE}}$).

Chapter 5 Conclusions

The goal of this study is to eventually create a geometry that could move up and down within a fluidized bed, breaking up agglomerations, through the manipulation of the inlet flow rate. Complications arose when objects that should sink based on densities did not do so due to the development of a de-fluidized region of particles above the submerged object. It was necessary to determine the properties of the de-fluidized region as to minimize its effect. In this step, the forces acting on a sphere in a fluidized bed have been predicted and verified. In doing so, the weight of the previously reported de-fluidized hood has been directly measured. From these direct measurements a prediction of the hood shape was extracted. The findings will now be compared to the results presented by past researchers, most notably Grace and Hosney, Hager and Schrag, Kulkarni, and Rees. Discussions on the causes and the meaning of the hood shape will follow.

5.1 Comparison to Past Work

Figure 31 compares this work's hood shape with those used by Rees and Hager and Schrag. The hood shown currently does vary from what has been previously observed. The method by which the hood size and shape was attained here is quite different from previous researchers' work. By determining the hood weight first and back calculating the associated volume, the current hood has been estimated through direct experimental results. In all previously found cases, the hood size and shape were determined through visual observation. Darkened fluidizing medium was placed on top of the bed such that

the hood top could be outlined. Pictures were then taken of the hood and estimates of the hood size and shape were made. The direct measurement technique, rather than visual observation, used in the current study could be a reason for the difference in hood shapes.

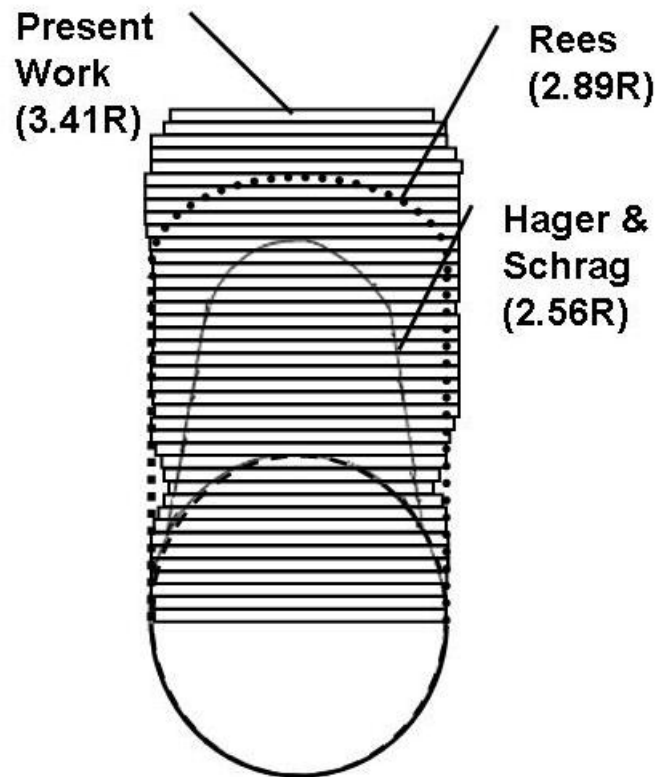


Figure 31: Comparison of hood shapes

Additionally, the differences between the hood shape presented here and those presented by Hager and Schrag could lie in the fact that they used perfectly spherical glass beads. Compared to the ground particles used in the current study, the beads will exhibit different packing characteristics as well as reduced friction between adjacent beads thus allowing for beads to roll off the hood. This would lead to a lower sloped hood as well as a shorter hood. Additionally, Hager and Schrag used a rectangular bed in their studies. This could lead to asymmetric flow structures within the bed which may impact the shape

of the hood. The hood presented here is qualitatively in agreement with that proposed by Rees. The difference in height could be attributed to the flow rates used. In Rees' work, bubbling to slugging flow rates were used, which are much higher than those used in the present work.

The hood height reported here is $3.41R_{\text{SPHERE}}$ above the centerline of the sphere or 1.7 times the diameter. This is within the range of reported hood heights in the literature. Hager and Schrag reported 0.8 times the diameter of the sphere whereas Glass and Harrison reported that it could be up to 4 times the diameter of the sphere. With a hood height of $3.41R_{\text{SPHERE}}$, the angle to which the hood rises is approximately 74.25° . This angle, referred to as the incidence angle by Rees, is the angle occupied by the outer edge of the submerged sphere at the equator to the center-top of the hood. Table 1 compares the hood heights and incidence angles.

	Hood Height	Incident Angle
Current Work	$3.41R$	74.25°
Rees (2005)	$2.89R$	70.69°
Kulkarni (1987)	$1.14R$	62.12°
Hager and Schrag (1976)	$2.56R$	68.66°

Table 1: Comparison of hood heights and incidence angles

The differences between the current work and Hager and Schrag and Rees have already been discussed. Kulkarni's work differs from the current finding in that he uses a rectangular bed with spherical beads. Also, the values taken from Kulkarni's work were

measured off of pictures of the hood. As Kulkarni himself explains, determining the boundary between the fluidized and de-fluidized regions in these pictures is very tough.

For the case of 40% flow, the hood ceased to grow at $4R$. This made the hood height $2.25R$. With a base diameter of $1.5R$, this made the incidence angle 72° . Thus, the hood size reduced with reduced velocity. While increasing the flow rate past bubbling would seem to reduce the hood size because it would agitate the hood, thus knocking it down, decreasing the flow rate to the minimum fluidization velocity would also seem to decrease the hood size because it would not allow for the bubbles to transport particles to the top of the hood. As will be discussed in section 5.2, the flow pattern created by the bubbles may be the method by which the hood grows.

Finally, with the hood weight now determined, we can verify Equation 14 as proposed by Grace and Hosney. This equation was meant to alter the buoyant force to account for the de-fluidized hood. The comparison is shown in Figure 32.

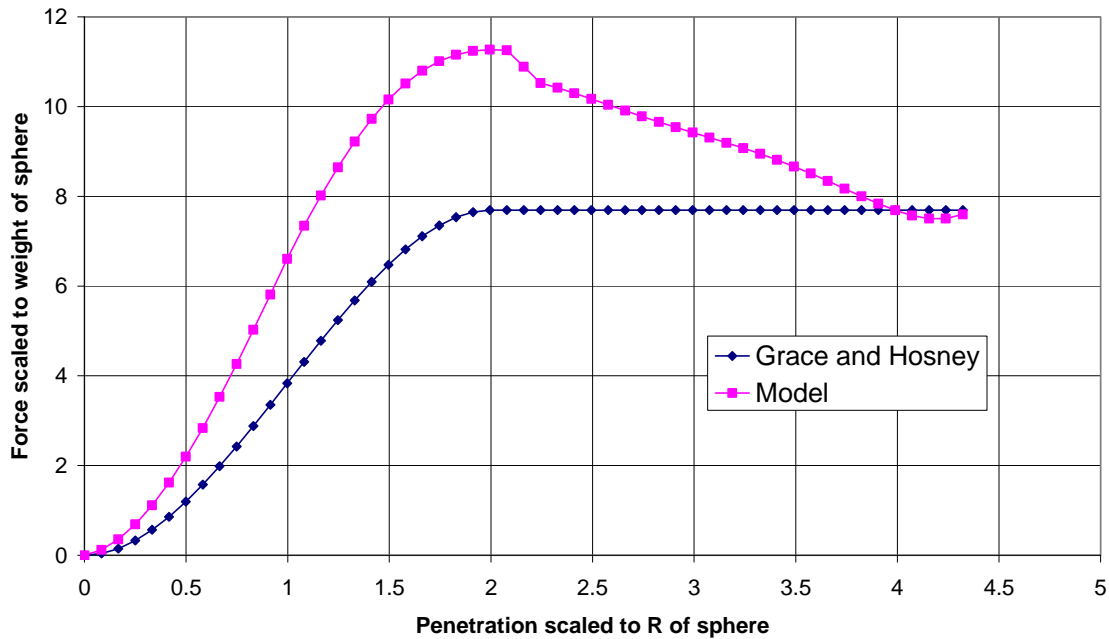


Figure 32: Comparison of model to Grace and Hosney for 1.5 U_{mf} case

The final forces agree between the two models. However, there is discrepancy in the manner in which the hood is shown to grow with increased penetration. However, Grace and Hosney were studying the forces on a stationary object already submerged in a fluidized bed. Therefore, the force of interest was the final force rather than the growth of forces as the hood grows.

5.2 Discussion on Hood Shape

The hood shape extracted from the data shows a relatively abrupt change from de-fluidized to fluidized. Before beginning the investigation into the hood shape, it was anticipated that the hood would more closely resemble a cone, with the de-fluidized

hood tailing off as the flow around the sphere moves downstream of the sphere and re-stabilizes. It was initially thought that the angle of repose of alumina oxide would represent the highest incidence angle. Once the hood was built to this angle, any additional alumina oxide accumulation would slide off of the hood. However, the angle of repose was found to be 44° . This is in agreement with the findings of Jaeger (1989) who reported an angle of repose of 39° for alumina oxide. As stated, the angle of incidence of the hood was found to be 74.25° , much greater than the angle of repose. The steep slope of the hood led to the question of why the hood would stop abruptly and is it believable for this discontinuity in the flow past the sphere to exist. An attempt to verify the latter was made through visual observations of the hood and its growth as the sphere was lowered. Figure 33 shows a view of the top of the bed at different sphere depths for the $1.5U_{mf}$ case. The deadened de-fluidized area can clearly be seen in the $h = R_{SPHERE}$ picture. The bubbles form a ring that encircles the submerged sphere. The edge of the de-fluidized hood is outlined as the darkened circle inside the bubble ring. Within this de-fluidized region, hills and valleys of alumina oxide can be seen. As the submerged sphere is lowered, the darkened line becomes fainter, the hills and valleys become flatter, and the bubbles become larger. By the last picture, at $4.61 R_{SPHERE}$, the deadened area resembles the rest of the bed and can be assumed to be fluidized.

However, the ring of bubbles that form around the sphere is evident throughout the series of pictures.

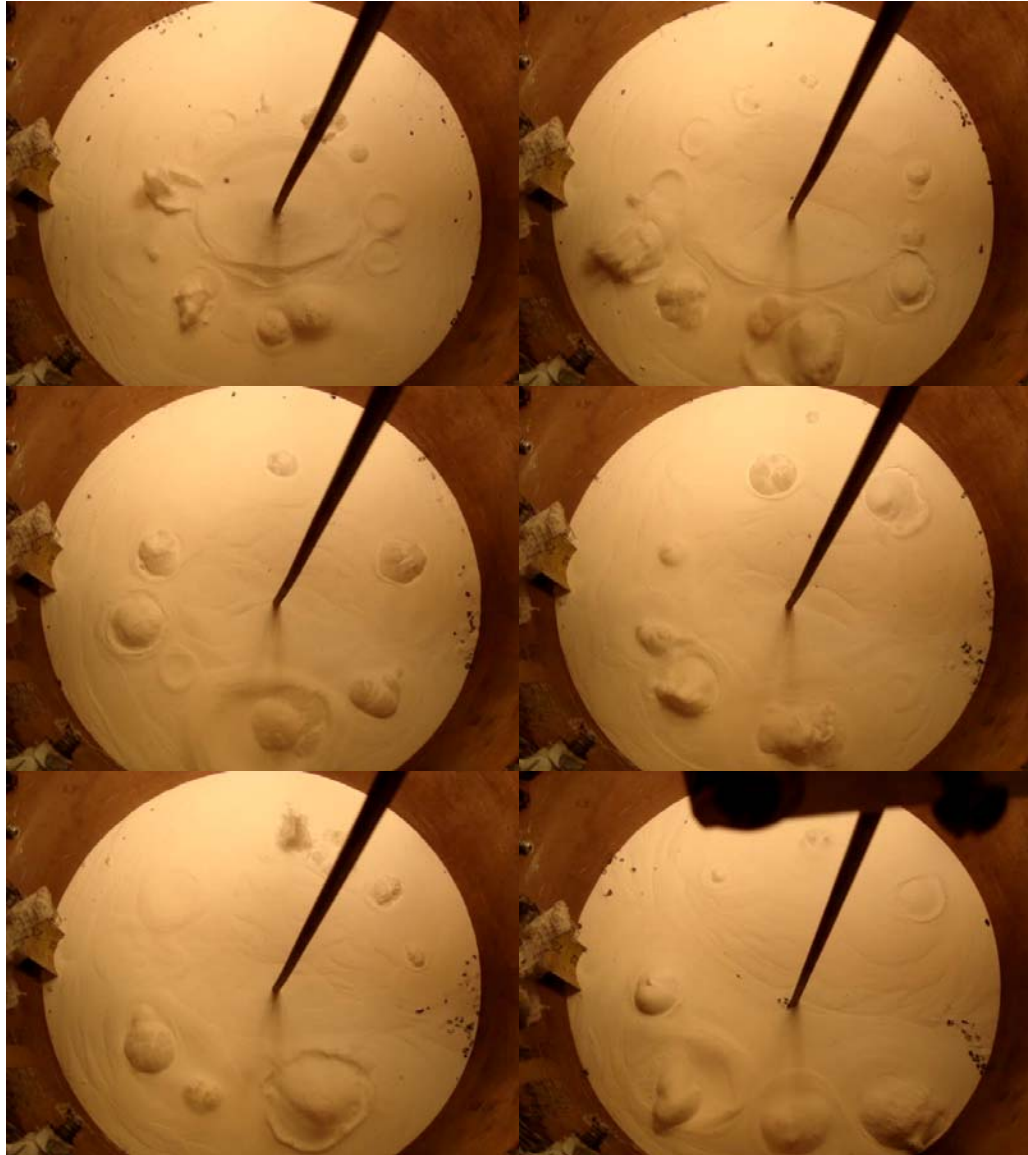


Figure 33: From top left to Bottom Right: Hood at 1R, 2R, 2.94R, 3.34R, 3.61R, 4.16R. The bubbles form a ring that encircles the submerged sphere. The edge of the de-fluidized hood can be seen as the darkened circle inside the bubble ring. As the submerged sphere is lowered, the darkened line becomes fainter and the bubbles become larger.

The voidages pull material along with them as they rise. When these voidages reach the surface, they “burst” and release the entrained material, “spewing” it over the bed surface. The explosion of each bubble has a radius which is directly proportional to the radius of the bubble. A larger bubble will lead to a larger explosion radius which will spew particles further away from the explosion site.

In the current case, the sphere causes voidages by accelerating the flow of interstitial gas around the sphere. These bubbles, upon collapsing at the surface would transport particles in all directions. Since the bubbles were aligned in a ring, the region within the ring would receive a high concentration of particles from the bubble explosions. This region was dead and the particles transported here would remain still. This transport would continue, adding more and more particles to the de-fluidized region, until the bubbles reached a large enough size, such that upon collapse, the particles were transported across the dead region. At this point, particle motion was created in the de-fluidized region.

In the region between this bubble ring and the bed walls, particles would move up with the bubbles, burst and then move out towards the bed wall. Upon hitting the walls, particles would get pulled down back into the bed. Eventually, the particles would be re-entrained in the bubbles and reappear in a bubble explosion. This circulation is common for a bubbling fluidized bed. However, juxtaposed to the inward circulation of particles on to the hood, a bed with two counteracting patterns of particle circulation is created. An illustration of this phenomenon is provided in Figure 34.

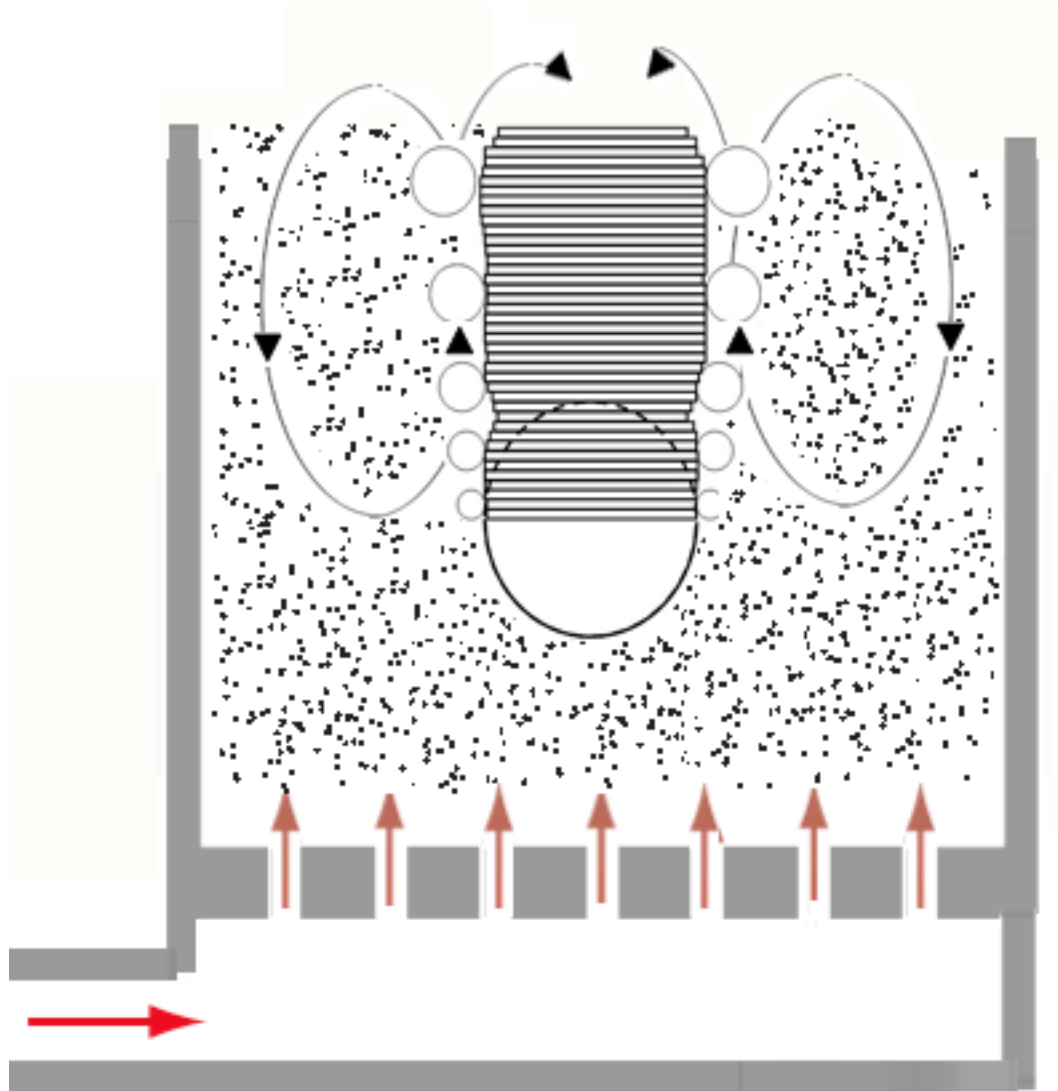


Figure 34: Diagram of the secondary circulation leading the de-fluidized hood growth. Voids travel from the hemisphere to the surface of the bed. Upon collapsing at the surface, particles entrained in the voids travel towards the walls and center of the bed. Arrows indicate the direction of particle flow

A gap in the horizontal direction between the bubble explosion site and the sphere edge could be observed. This indicated that the bubbles will surface at a distance

away from the sphere circumference laterally. This could either mean that the bubbles shoot out at an angle away from the sphere or that they exhibit preferential growth on the side of the bubbles adjacent to the fluidized section of the bed. Assuming the latter since there is no justification for the former, the bubbles would transport particles from the fluidized section of the bed, rather than from the de-fluidized section. This may be the means by which the hood grows: by bubbles created due to the flow acceleration imposed by the submerged objects carrying particles from the fluidized section to the top of the hood. This same pattern was observed by Hager and Schrag as well (Figure 4). Furthermore, the hood ceases to grow once the bubbles are large enough such that their explosion radius is sufficient to carry particles across the dead hood. At this point, when $R_{\text{EXPLOSION}} > R_{\text{SPHERE}}$, the hood will stop growing as particles can be transported across the hood, thus giving motion to the top of the de-fluidized region. This seems to explain the abrupt end in the hood growth – the hood will stop growing once the bubbles caused by the submerged sphere are large enough to re-fluidize the de-fluidized hood.

Nomenclature

Greek Symbols:

ε	the bed voidage
ρ_p	the density of the particles
ρ_g	the density of the gas
ρ_f	the density of the fluidized bed
ρ_s	the density of the dead bed
μ_f	the fluid viscosity
φ	the sphericity which is the ratio of the surface area of a sphere of the same volume as the particle to the surface area of the particle
Δ	shape correction factor for the total particle

English Symbols:

A	the cross sectional area of the bed
$A(z)$	the submerged surface area of the sphere at the penetration depth z
Ar	the Archimedes number
C_D	the drag coefficient
d	the diameter of the immersed object
d_m	the mean particle diameter
d_s	the diameter of a particle with the same surface area as the actual particle
D_{wetted}	the wetted diameter of the sphere at the penetration height, h

f	drag coefficient correction
F_B	the buoyant force
g	the acceleration due to gravity
\tilde{g}	gravitational acceleration when buoyancy is considered
h	the penetration depth of the submerged objects into the fluidized bed
H_{hood}	the height of the de-fluidized hood
k_w	the wall correction factor
L	the bed height
M	the mass of the particles
n	the particle number density
∇p	the pressure gradient around the object
p_b	the pressure drop through the bed
R_{FB}	the radius of the fluidized bed
R_{SPHERE}	the radius of the sphere
Re	the Reynolds number
U	the fluidization velocity
U_{mf}	the minimum fluidization velocity
U_T	the velocity tangential to sphere
U_1	the velocity of the interstitial gas at an object penetration of h
V	the volume of the object immersed in the fluid
V_{bed}	the volume of the bed using the predicted bed height
V_{HOOD}	the volume of the hood
Vol_t	the total volume of the particle and hood

References

- Asif, M. (1998), "Segregation velocity model for fluidized suspension of binary mixture of particles," *Chemical Engineering and Processing*, 37, pp. 279 – 287.
- Batchelor, G.K. (1988), "A new theory of the instability of a uniform fluidized bed," *Journal of Fluid Mechanics*, 193, pp. 75 – 110.
- Bowen, B.D. and Masliyah, J.H. (1973), "Drag force on axisymmetric particles in Stokes' flow," *The Canadian Journal of Chemical Engineering*, 51, pp. 8-15.
- Clift, R. and Gauvin, W.H. (1970), "The motion of particles in turbulent gas streams," *Proc. Chemeca*, 1, pp. 14.
- Crowe, C., Sommerfield, M. and Tsuji, Y. (1998), *Multiphase Flows with Droplets and Particles*, CRC Press, New York.
- Davidson, J.F., Harrison, D. and Guedes de Carvalho, J.R.F. (1977), "On the Liquidlike Behavior of Fluidized Beds," *Annual Review of Fluid Mechanics*, 9, pp. 55 – 86.
- Liu, F. and Orr, C. (1960), "Apparent Viscosity of Gas-Solid Fluidized Systems," *Journal of Chemical and Engineering Data*, 5, pp. 430 – 432.
- Gilbertson, M.A. and Eames, I. (2001), "Segregation patterns in gas-fluidized systems," *Journal of Fluid Mechanics*, 433, pp.347 – 356.
- Glass, D.H., and Harrison, D. (1964), "Flow patterns near a solid obstacle in a fluidized bed," *Chemical Engineering Science*, 19, pp. 1001 – 1002.
- Grace, J.R. and Hosney, N. (1985), "Forces on horizontal tubes in gas fluidised beds," *Chem. Eng. Res. Des.*, 63, pp. 191 – 198.
- Hager, W.R., and Schrag, S.D. (1976), "Particle circulation downstream from a tube immersed in a fluidized bed," *Chemical Engineering Science*, 31, pp. 657 – 659.
- Howard, JR (1989), *Fluidized Bed Technology: Principles and Applications*, Adam Hilger, New York.
- Huilin, L., Yurong, H., Gidaspow, D., Lidan, Y. and Yukun, Q. (2003), "Size segregation of binary mixture of solids in bubbling fluidized beds," *Powder Technology*, 134, pp. 86 – 97.

Jackson, Roy (2000), *The Dynamics of Fluidized Particles*, Cambridge University Press, New York.

Jaeger, H.M., Liu C. and Nagel S.R. (1989), "Relaxation at the angle of repose," *Physical Review Letters*, 62, pp. 40-43.

Kulkarni, A. (1987), "Defluidized zone over a horizontally immersed tube in a fluidized bed," *Chemical Engineering Science*, 42, pp. 1245 – 1247.

Marzocchella, A., Salatino, P., Di Pastena, V. and Lirer, L. (2000), "Transient fluidization and segregation of binary mixtures of particles," *AIChE Journal*, 46, 2175 – 2182.

Mehrani, P. and Hsiaotao, T.B., Grace, J. (2005), "Electrostatic charge generation in gas-solid fluidized beds," *Journal of Electrostatics*, 63, pp.165 – 173.

Mostoufi ,N. and Chaouki, J. (1999), "Prediction of effective drag coefficient in fluidized beds," *Chemical Engineering Science*, 54, pp. 851 – 858.

Oshitani, J., Trisakti, B. and Tanaka, Z. (2001), "Evaluation of fluidized particle flow by measurement of apparent buoyancy," *Advanced Powder Technology*, 12, pp. 95 – 104.

Perry, R.H. and Green, D.W. (1998), *Perry's Chemical Engineers' Handbook*, McGraw-Hill, New York.

Qiaoqun, S., Huilin, L., Wentie, L., Yurong, H., Lidan, Y. and Gidaspow, D., (2005), "Simulation and experiment of segregating/mixing of rice husk-sand mixture in a bubbling fluidized bed," *Fuel*, 84, pp. 1739 – 1748.

Rees, A.C., Davidson, J.F., Dennis, J.S. and Hayhurst, A.N. (2005), "The rise of a buoyant sphere in a gas-fluidized bed," *Chemical Engineering Science*, 60, pp. 1143 – 1153.

Rees, A.C., Davidson, J.F., Dennis, J.S. and Hayhurst, A.N. (2007), "The apparent viscosity of the particulate phase of the bubbling gas-fluidized beds: A comparison of the falling or rising sphere technique with other methods," *Chemical Engineering Research and Design*, 85, pp.1341 – 1347.

Tee, S., Mucha, P.J., Brenner, M.P. and Weitz, D.A. (2008), "Velocity fluctuations in a low Reynolds-number fluidized bed," *Journal of Fluid Mechanics*, 596, pp. 467 – 475.